1 The Mediterranean forecasting system.

2 Part I: evolution and performance

3 Giovanni Coppini[1,*], Emanuela Clementi[2], Gianpiero Cossarini[3], Stefano Salon[3], Gerasimos Korres[4],
4 Michalis Ravdas[4], Rita Lecci[1], Jenny Pistoia[2], Anna Chiara Goglio[2], Massimiliano Drudi[1], Alessandro
5 Grandi[1], Ali Aydogdu[2], Romain Escudier[2,5], Andrea Cipollone[2], Vladislav Lyubartsev[1], Antonio
6 Mariani[1], Sergio Cretì[1], Francesco Palermo[1], Matteo Scuro[1], Simona Masina[2], Nadia Pinardi[6,7], Antonio
7 Navarra[6,8], Damiano Delrosso[9], Anna Teruzzi[3], Valeria Di Biagio[3], Giorgio Bolzon[3], Laura Feudale[3],
8 Gianluca Coidessa[3], Carolina Amadio[3], Alberto Brosich[3], Arnau Miró[10], Eva Alvarez[3], Paolo Lazzari[3],
9 Cosimo Solidoro[3], Charikleia Oikonomou[4], Anna Zacharioudaki[4]

10 [1] Ocean Predictions and Applications Division, Fondazione Centro Euro-Mediterraneo sui Cambiamenti Climatici (CMCC),
11 Italy
12 [2] Ocean Modeling and Data Assimilation Division, Centro Euro-Mediterraneo sui Cambiamenti Climatici (CMCC), Italy
13 [3] Istituto Nazionale di Oceanografia e di Geofisica Sperimentale (OGS), Italy
14 [4] Hellenic Centre for Marine Research (HCMR), Greece
15 [5] Mercator Océan International, France
16 [6] Centro Euro-Mediterraneo sui Cambiamenti Climatici (CMCC), Bologna, Italy
17 [7] Department of Physics and Astronomy, Università di Bologna, Bologna, Italy
18 [8] Department of Biological, Geological and Environmental Sciences (BIGEA), Università di Bologna, Bologna, Italy
19 [9] Istituto Nazionale di Geofisica e Vulcanologia (INGV), Italy
20 [10] Barcelona Supercomputing Center, Barcelona (BSC), Spain

21 *Correspondence to*: Giovanni Coppini giovanni.coppini@cmcc.it

22 **Abstract.** The Mediterranean Forecasting Systems produces operational analyses, reanalyses and 10-day forecasts for many

23 Essential Ocean Variables (EOVs), from currents, temperature to wind waves and pelagic biogeochemistry. The products are

24 available at a horizontal resolution of 1/24 degrees (approximately 4 km) and 141 unevenly spaced vertical levels.

25 The core of the Mediterranean Forecasting System is constituted by the physical (PHY), the biogeochemical (BIO) and the

26 wave (WAV) components coupled offline, consisting of both numerical models and data assimilation modules. The 3

27 components together constitute the so-called Mediterranean Monitoring and Forecasting Center (Med-MFC) of the Copernicus

28 Marine Service.

29 Daily 10-day forecasts are produced by the PHY, BIO and WAV components as well as analyses, while reanalyses are

30 produced for the past 30 years about every ~3 years and extended (yearly). The modelling systems, their coupling strategy and

31 evolution is illustrated in detail. For the first time, the quality of the products is documented in terms of skill metrics evaluated

32 on a common three-year period (2018-2020), giving the first complete assessment of uncertainties for all the Mediterranean

33 environmental variable analyses.

1 Introduction

Ocean analysis and forecasting systems are now available for the global and world ocean regional seas at different spatial scales and with different numbers of Essential Ocean Variables (EOV) considered (Tonani et al., 2015). The societal drivers for the operational products stemming out of the ocean analysis and forecasting products are the safety of maritime transport, multiple coastal hazards and climate anomalies. Moreover, the operational products are at the basis of new understanding of the dynamics of the ocean circulation (Pinardi et al., 2015), its linked biogeochemical cycles, among others, carbon uptake and eutrophication (Melaku Kanu et al., 2015, von Schuckmann et al., 2020) and extreme storm surge events (Giesen et al., 2021). The ocean analysis and forecasting system for the entire Mediterranean Sea was set up in the past 15 years (Pinardi and Coppini, 2010; Pinardi et al., 2017; Lazzari et al., 2010; Salon et al., 2019; Ravdas et al., 2018; Katsafados et al. 2016). In this paper we give an overview of the "core" components of the system, i.e., the numerical models and the data assimilation modules that represent the eddy-resolving ocean general circulation, the biogeochemical tracers and the wind waves. Furthermore, we will document the quality EOV products using goodness indices (Brassington et al., 2017). The core components constitute the so-called Mediterranean Monitoring and Forecasting Center (Med-MFC) of Copernicus Marine Service (Le Traon PY et al., 2019). The integrated approach of MED-MFC system represents a unique opportunity for the users who are able to access state-of-the-art data coupled and provided in a uniform manner (e.g., same grid, unique format, unique point of access).

This ocean analysis and forecasting system, hereafter Med-MFC, produces analyses, 10 days forecasts and reanalysis (Adani et al., 2011; Pinardi et al., 2015; von Schckumann et al., 2016; von Schckumann et al., 2018; von Schckumann et al., 2019; Terzic et al., 2021, Simoncelli et al., 2016; Simoncelli et al., 2019; Ravdas et al., 2018, Escudier et al., 2020; Escudier et al., 2021).

The Mediterranean Sea is a semi-enclosed basin with an anti-estuarine circulation corresponding to a 0.9/0.8 Sv baroclinic inflow/outflow at the Strait of Gibraltar, positive energy inputs by the winds, net buoyancy losses inducing a vigorous overturning circulation (Cessi et al., 2014; Pinardi et al., 2019). The basin scale circulation is dominated by mesoscale and sub-mesoscales variability (Pinardi et al., 2016; Bergamasco et al., 2010; Pinardi et al., 2006; Robinson et al., 2001; Ayoub et al., 1998), the former subdivided into semi-permanent and synoptic mesoscales with a spatial scale larger than 4-6 times the local Rossby radius of deformation (Terzic et al., 2021). The stratification is large during the summer in the first 50 meters and during winter the water column is practically unstratified. The Mediterranean Sea is an oligotrophic basin (Siokou-Frangou et al., 2010) with a west-to-east decreasing productivity gradient (Lazzari et al., 2012) and relatively high primary productivity in open ocean areas where winter mixing increases surface nutrients (Cossarini et al., 2019). The wave conditions are driven by the winter storminess, while summer is characterised by low significant wave height values and higher value scatter (Ravdas et al., 2018). Mean wave periods are around 5 s and mean significant wave height is 3 m.

In this paper we describe the final set up of the Med-MFC core components for the period 2017-2020: The PHY component is offline coupled daily to the biochemical and wave components. This allows several model parametrizations to be calibrated

67 to obtain the best result in term of the specific environmental variable considered by each component. Furthermore, this weakly

68 coupled system ensures an efficient development of the data assimilation modules connected to each numerical model modules

69 and specific input data sets. It is a distributed system that shares information when and how it is required by relevant processes,

70 with efficiency and effectiveness. Due its rather unique structure and the quality of its products the system described could be

71 used as a basic standard for new systems to be developed.

72 The paper is organised as follows. Section 2 overviews the technical specifications of the Med-MFC components, Section 3

73 describes the quality of the system for a reference period from 2018 to 2020, Section 4 concludes the paper and presents future

74 perspectives.

2. Description of the Med-MFC core components

75

76 The structure of the Med-MFC core components is shown in Figure 1: the physical component (PHY) is composed of the

77 NEMO general circulation model (Madec et al., 2019) coupled to the WaveWatch-III (WW3) wave model (Clementi et al.,

78 2017a) and the ocean data assimilation OceanVar 3DVAR (ref); the biogeochemical component (BIO) is composed of the

79 Biogeochemical Flux Model (BFM), the tracer transport (OGSTM) and a data assimilation scheme (Lazzari et al., 2012;

80 Lazzari et al., 2016 Cossarini et al., 2015; Vichi et al., 2020), coupled daily to the daily mean of the PHY component fields;

81 the wave component (WAV) is composed of the wave model WAM (AMDI Group, 1988) and its assimilation scheme, coupled

82 daily to the daily mean of the PHY components fields. Daily 10 days forecasts are produced with all PHY, BIO and WAVE

83 components as well as analyses and reanalyses as described below.

2.1. The general circulation model component

84

2.1.1. Numerical model description

85

86 The PHY numerical model component comprises a two-way coupled current-wave model based on NEMO and WW3

87 implemented over the whole Mediterranean basin and extended into the Atlantic Sea in order to better resolve the exchanges

88 with the Atlantic Ocean (Figure 2). The model horizontal grid resolution is 1/24° (ca. 4 km) and is resolved along 141 unevenly

89 spaced vertical levels (Clementi et al., 2017b; Clementi et al., 2019). The topography is an interpolation of the GEBCO 30arc-

90 second grid (http://www.gebco.net/data_and_products/gridded_bathymetry_data/gebco_30_second_grid/), filtered and

91 specifically modified in critical areas such as: the Eastern Adriatic coastal areas, Gibraltar and Messina straits, Atlantic external

92 border. All the numerical model choices are documented in Table A1.

93 The general circulation model considers the non-linear free surface formulation and vertical z-star coordinates. The numerical

94 scheme uses the time-splitting formulation to solve the free surface and the barotropic equations with a (100 times) smaller

95 time step with respect to the one used to evaluate the prognostic 3D variables (240 seconds). The active tracers (temperature

96 and salinity) advection scheme is a mixed up-stream/MUSCL (Monotonic Upwind Scheme for Conservation Laws; Levy et

97 al., 2001) as modified in Oddo et al. (2009). The vertical diffusion and viscosity terms are defined as a function of the

98   Richardson number, following Pacanowski and Philander (1981). The air-sea surface fluxes of momentum, mass, and heat are

99   computed using bulk formulae described in Pettenuzzo et al. (2010) and the Copernicus satellite gridded SST data (Buongiorno

100 Nardelli et al., 2013) is used to correct the non-solar heat flux using a relaxation constant of 110 $Wm^{-2}K^{-1}$ centred at midnight.

101 A detailed description of other specific features of the model implementations can be found in Tonani et al., (2008), Oddo et

102 al. (2009), and Oddo et al. (2014).

103 The wave model WW3 is discretized by means of 24 directional bins (15° resolution) and 30 frequency bins (ranging between

104 0.05 Hz and 0.7931 Hz) to represent the wave spectral distribution. The wave model is implemented using the same bathymetry

105 and grid of the hydrodynamic model and uses the surface currents to evaluate the wave refraction, but assumes no interactions

106 with the ocean bottom. The Mediterranean implementation of WW3 follows WAM cycle4 model physics (Gunter et al., 1993);

107 the wind input and dissipation terms are based on Janssen's quasi-linear theory for wind-wave generation (Jansen, 1989;

108 Jansen, 1991), the wave dissipation term is based on Hasselmann (1974) whitecapping theory according to Komen et al. (1984)

109 and the non-linear wave-wave interaction is modelled using the Discrete Interaction Approximation (DIA, Hasselmann et al.,

110 1985). The exchanges between the hydrodynamic and wave models are performed using an online hourly two-way coupling

111 which provides to WW3 the air-sea temperature difference and the surface currents evaluated by NEMO, while the neutral

112 drag coefficient estimated in WW3 is sent to NEMO to evaluate the surface wind stress.

113 The NEMO-WW3 coupled system is intended to provide the representation of current-wave interaction processes in the ocean

114 general circulation. At the moment the feedback is considered only for the surface wind stress drag coefficient and more details

115 on this wave-current model coupling can be found in Clementi et al. (2017).

116   2.1.2. Model initialization, external forcing and boundary conditions

117 The PHY component was initialised in January 2015 using temperature and salinity winter climatological fields from WOA13

118 V2 (World Ocean Atlas 2013 V2, https://www.nodc.noaa.gov/OC5/woa13/woa13data.html). The atmospheric forcing fields

119 for both NEMO and WW3 models are from 6 hours (3 hours for the first 3 days of forecast), 0.125° horizontal resolution

120 operational analysis and forecast fields from the European Centre for Medium-Range Weather Forecast (ECMWF); a higher

121 spatial (0.1° in horizontal) and temporal resolution dataset is used starting from year 2020.

122 The general circulation model lateral open boundary conditions (LOBC) in the Atlantic Ocean are provided by the Copernicus

123 Global Analysis and Forecast products (Lellouche et al., 2018) at 1/12° horizontal resolution and 50 vertical levels. The

124 Dardanelles Strait boundary conditions (Delrosso, 2020) consist of a merge between the Copernicus global ocean products and

125 daily climatology derived from a Marmara Sea box model (Maderich et al., 2015). The WW3 model implementation considers

126 closed boundaries in both Atlantic Ocean and Dardanelles strait.

127 The river runoff inputs consist of monthly climatological data for 39 major rivers (characterised by an average discharge larger

128 than 50 m^{3}/s) with a prescribed constant salinity at river mouth (Delrosso, 2020) and listed in Table A.4.

129 **2.1.3 The data assimilation component**

130 A 3D-variational data assimilation scheme, called OceanVar, initially developed by Dobricic and Pinardi (2008)) and further

131 improved for a wide range of ocean data assimilation applications (Storto et al., 2015) is coupled to NEMO.

132 The OceanVar scheme aims to minimise the cost function as described in the following Eq. (1):

133

134
$$J = \frac{1}{2}\delta x^T B^{-1}\delta x + \frac{1}{2}(H\delta x - d)^T R^{-1}(H\delta x - d),$$ (1)

135

136 where $\delta x = x - x_b$, and x is the unknown ocean state, equal to the analysis x_a at the minimum of J, x_b is the background

137 state, $d = y - H(x_b)$ is the misfit between an observation y and its modelled correspondent mapped onto the observation

138 space to the observation location by the observation operator, H.

139 In OceanVar, the background error covariance matrix is considered as $B = VV^T$, where V is a sequence of linear operators:

140 $V = V_\eta V_H V_V$. Multivariate EOFs (Empirical Orthogonal Functions) (Dobricic et al., 2006; Pistoia et al., 2017) compose the

141 vertical component operator, V_V. EOFs are computed in every grid point for the sea surface height, temperature and salinity

142 using a three-year simulation in order to capture the mesoscale eddy variability that is assumed to represent the unbalanced

143 component of the background error covariance. The horizontal covariances, V_H, are modelled by an iterative recursive filter

144 (Dobric and Pinardi, 2008, Storto et al., 2014). In order to assimilate altimeter observations, the dynamic height operator, V_η,

145 developed in Storto et al., (2011) is used. A reference level of 1000 m is used for this operator so SLA along track observations

146 shallower than this depth are not assimilated.

147 The observational error covariance matrix, R, is estimated following Desroziers et al. (2005) relationship. The assimilated

148 observations include along-track altimeter sea level anomaly from six satellites and in-situ vertical temperature and salinity

149 profiles from Argo floats. A special quality control procedure is applied to the Argo data before they are assimilated. It consists

150 of removing not good quality profiles, rejecting observations with negative temperature and/or salinity, temperature higher

151 than 45ºC and salinity higher than 45PSU, removing profiles with gaps in the observations of more than 40m in the first 300m

152 depth (to avoid possible inconsistencies in the thermocline), profiles with observations provided only below 35m depth and

153 observations in the 1ˢᵗ model layer (0-2m). Moreover, a background quality check is implemented to reject observations whose

154 square departure exceeds the sum of the observational and background-error variances 64 times in case of SLA and 25 times

155 in case of *in-situ* temperature and salinity.

156 The misfits are computed at the observation time by applying the FGAT (First Guess at the Appropriate Time) procedure and

157 the corrections to the background are applied once a day, using observations within a one-day time window.

2.2. The wind wave component

2.2.1. Numerical model description

The WAV component consists of two nested wave model implementations: the first grid covers the whole Mediterranean Sea at 1/24° horizontal resolution and it is nested within a coarser resolution wave model grid at 1/6° horizontal resolution implemented over the Atlantic Ocean (Figure 2).

The wave model is based on the state-of-the-art third generation WAM Cycle 4.6.2 which is a modernised and improved version of the well-known and extensively used WAM Cycle 4 wave model (AMDI Group, 1988; Komen at al., 1994). WAM solves the wave transport equation explicitly without any presumption on the shape of the wave spectrum. Its source terms include the wind input, whitecapping dissipation, nonlinear transfer, and bottom friction. The wind input term is adopted from (Snyder et al., 1981). The whitecapping dissipation term is based on (Hasselman, 1974) whitecapping theory. The wind input and whitecapping dissipation source terms of the present cycle of the wave model are a further development based on Janssen´s quasi-linear theory of wind-wave generation (Jansen, 1989; Jansen, 1991). The nonlinear transfer term is a parameterization of the exact nonlinear interactions as proposed by (Komen et al., 1984) and (Hasselman et al., 1985). Lastly, the bottom friction term is based on the empirical JONSWAP model of (Hasselman et al., 1973).

The bathymetric map has been constructed using the GEBCO 30arc-second bathymetric data set for the Mediterranean Sea model and the ETOPO 2 data set (U.S. Department of Commerce, National Oceanic and Atmospheric Administration, National Geophysical Data Centre, 2006. 2-minute Gridded Global Relief Data) for the North Atlantic model. In both cases mapping on the model grid was done using bi-linear interpolation accompanied by some degree of isotropic Laplacian smoothing. This bathymetry is different from the one used for the PHY component, optimized for the specific quality of the wave products.

The wave spectrum is discretized using 32 frequencies, which cover a logarithmically scaled frequency band from 0.04177 Hz to 0.8018 Hz (covering wave periods ranging from approximately 1 s to 24 s) at intervals of $df/f = 0.1$ and 24 equally spaced directions (15 degrees bin). The WAV model component runs in shallow water mode considering wave refraction due to depth and currents in addition to depth-induced wave breaking. Modifications from default values of WAM 4.6.2 have been performed in the input source functions as a result of a tuning procedure. Specifically, the value of the wave age shift parameter (ZALP) in the wind input source function was set to 0.011 (0.008 is the default) for the Mediterranean model and the tunable whitecapping dissipation coefficients C_{DS} and δ were altered from their default values to become $C_{DS}=1.33$ (2.1 default) and $\delta = 0.5$ (default value was 0.6). Finally, a limitation to the high-frequency part of the wave spectrum corresponding to the Cy43r1 ECMWF wave forecasting system (ECMWF, 2016) was also implemented and tested in order to reduce the wave steepness at very high wind speeds.

2.2.2. Model initialization, external forcing and boundary conditions

The WAV component is forced with 10 m above sea surface wind fields obtained from the ECMWF Integrated Forecasting System (IFS) at 1/8° dissemination resolution. The temporal resolution of the wind forcing is 3 h for the first 3 days of the

191   forecast and 6 h for the rest of the forecast cycle. The wind is bi-linearly interpolated onto the model grids. Sea ice coverage

192   fields are also obtained from ECMWF at the same horizontal resolution (1/8°) and are updated daily. With respect to currents

193   forcing, the WAV model is forced by daily averaged surface currents obtained from Copernicus Marine Service Med MFC at

194   1/24° resolution and the North Atlantic model is forced by daily averaged surface currents obtained from the Copernicus

195   Global wave model at 1/12° resolution.

196   The Mediterranean Sea model receives a full wave spectrum at 5-min intervals at its Atlantic Ocean open boundary from the

197   WAM implementation in the North Atlantic. The latter model is considered to have all its four boundaries closed assuming no

198   wave energy propagation from the adjacent seas. This assumption is readily justified for the north and west boundaries of the

199   North Atlantic model considering the adjacent topography which restricts the development and propagation of swell into the

200   model domain.

201

202   2.2.3 The wave data assimilation component

203   The assimilation module of the WAV component is based on the data assimilation scheme of WAM Cycle 4.6.2 which consists

204   of an Optimal Interpolation (OI) of the along-track Significant Wave Height (SWH) observations retrieved by altimetry and

205   then re-adjusting the wave spectrum at each grid point accordingly. This assimilation approach was initially developed by

206   Lionello et al. (1992) and consists of two steps. First, a best guess (analysed) field of significant wave height is determined by

207   OI with appropriate assumptions regarding the error covariance matrix. One of the key issues is the specification of the

208   background error covariance matrix, for the waves called P, and the observation error covariance matrix, R. The first is defined

209   as in the following Eq. (2):

210    $P = \exp\left(\dfrac{d_{ij}}{l_c}\right),$ (2)

211   while the second is Eq. (3):

213    $R = \dfrac{\sigma_o^2}{\sigma_b^2},$ (3)

215   where i and j are the model grid points in the longitudinal and latitudinal directions respectively, d is the distance of the

216   observation location to the grid point, l_c is the field correlation length, while σ_o^2 and σ_b^2 stand for the observation and model

217   errors, respectively. In the above expressions the error is considered as being homogeneous and isotropic. We use R=1 and the

218   correlation length l_c equal to 3 deg (~300 km).

219   Finally, the weights assigned to the observations are the elements of the gain matrix K as presented in Eq. (4):

221    $K = PH^T[HPH^T + R]^{-1},$ (4)

223 where H is the observation operator that projects the model solution to the observation location. For the current version of
224 Med-waves, the OI analysis procedure is applied only to altimeter along-track SWH measurements although wind at 10m
225 measurements can be assimilated as well.

226 During the second step, the analysed significant wave height field is used to retrieve the full dimensional wave spectrum from
227 a first-guess spectrum provided by the model itself, introducing additional assumptions to transform the information of a single
228 wave height spectrum into separate corrections for the wind sea and swell components of the spectrum. Two-dimensional wave
229 spectra are regarded either as wind sea spectra, if the wind sea energy is larger than 3/4 times the total energy, or, if this
230 condition is not satisfied, as swell. If the first-guess spectrum is mainly wind-sea, the spectrum is updated using empirical
231 energy growth curves from the model. In case of swell, the spectrum is updated assuming the average wave steepness provided
232 by the first-guess spectrum is correct, but the wind is not updated.

233 Prior to assimilation, all altimeter SWH observations are subject to a quality control procedure. Every day the system is
234 scheduled to simulate 264 hours: 24 hours in the past (analysis) blending through data assimilation model results with all
235 satellite SWH observations available followed by 240 hours forecast. The assimilation step adopted for the current version of
236 the Med-waves system equals to 3 hours.

2.3 Mediterranean biogeochemical component

2.3.1. Numerical model description

239 The BIO component consists of the Biogeochemical Flux Model (BFM, Vichi et al., 2007) coupled with the transport
240 (OGSTM) module (Salon et al., 2019). Advection, vertical and horizontal diffusion and the sinking term for the
241 biogeochemical tracers (Foujols et al., 2000) are solved by the OGSTM module that uses daily 3D velocity, diffusivities and
242 2D atmospheric fields provided by the PHY component through the offline coupling scheme (Figure 1). A source splitting
243 numerical time integration is used to couple advection and diffusion to the biochemical tracer rates.

244 BFM describes the biogeochemical cycles of carbon, nitrogen, phosphorus, silicon and oxygen through the dissolved inorganic
245 and the particulate living and non-living organic compartments (Lazzari et al., 2012; Lazzari et al., 2016). The model includes
246 four phytoplankton functional groups (i.e., diatoms, flagellates, picophytoplankton and dinoflagellates), four zooplankton
247 groups (i.e., carnivorous, and omnivorous mesozooplankton, heterotrophic nanoflagellates and microzooplankton) and
248 heterotrophic bacteria. Among the nutrients, dissolved inorganic nitrogen is simulated in terms of nitrate and ammonia. The
249 non-living dissolved organic compartment includes labile, semi-labile and refractory organic matter. A carbonate system
250 component (Cossarini et al., 2015) includes alkalinity (ALK), dissolved inorganic carbon (DIC) and particulate inorganic
251 carbon (PIC) as prognostics variables, computes CO_2 air-sea gas exchange according to Wanninkhof (2014) and provides
252 diagnostics variables such as pH, CO_2 concentration and calcite saturation horizon.

253

2.3.2. Model initialization, external forcing and boundary conditions

255 Climatological profiles from EMODnet (Buga et at., 2018) are used to initialize nutrients (nitrate, ammonia, silicate and
256 phosphate), oxygen and carbonate variables (DIC and alkalinity) in each of the areas represented in Fig. 3. The model has two
257 open lateral conditions: in the Atlantic Ocean and at the Dardanelles Strait. Nutrients, oxygen, DIC and alkalinity in the Atlantic
258 are provided through seasonally varying climatological profiles derived from Word Ocean Atlas (WOA 2018) and literature
259 (Alvarez et al., 2014) and Newtonian dumping is applied. A Dirichlet-type scheme with constant concentration values of
260 nutrients, DIC and alkalinity derived from literature (Yalcin et al., 2017; Tugrul et al., 2002; Souvermezoglou et al., 2014;
261 Copin-Montegut, 1993; Schneider et al., 2007; Krasakopoulou et al., 2017) is applied at the Dardanelles Strait. The
262 concentrations are also tuned to provide input fluxes from Black Sea to the Mediterranean Sea consistent with published
263 estimates (Deliverable of Perseus, 2020; Yalcin et al., 2017; Tugrul et al., 2002; Copin-Montegut, 1993). A radiative condition
264 is set for the other BFM tracers.
265 Terrestrial inputs include 39 rivers consistently with the PHY component. Annual nutrients input are about 46500 10^6 molN/y
266 and 881 10^6 molP/y e (Salon et al., 2019). Carbon and alkalinity inputs are 9300109 gC/y and 800 109 mol/y, respectively.
267 Estimates are derived considering typical concentrations per freshwater mass in macro coastal areas of the Mediterranean Sea
268 (Copin-Montegut, 1993; Meybech and Ragu, 1995; Kempe et al., 1991) and the river water discharges from the PERSEUS
269 dataset (Deliverable of Perseus, 2012 as before). Annual atmospheric nutrient depositions are 81300 10^6 molN/y and 1194 10^6
270 molP/y for nitrogen and phosphorus, respectively (Ribera d'Alcalà et al., 2003). Atmospheric pCO2 mean annual
271 concentrations are from the ENEA Lampedusa (Trisolino et al., 2021) station with the present-day values extrapolated by
272 linear regression.

2.3.3 The biogeochemical data assimilation component

274 The BIO component features a variational data assimilation scheme (3DVarBio) which is based on the minimization of the
275 cost function (Eq. 1) (Teruzzi et al., 2014). Minimization is computed iteratively in a reduced space using an efficient parallel
276 PETSc/TAO solver (Teruzzi et al., 2019) and the background error covariance matrix, B, is factorised in a sequence of linear
277 operators, as in the PHY component, that accounts for the vertical error covariance of the biogeochemical fields, the horizontal
278 error covariance, and the error covariance among the biogeochemical variables.
279 The horizontal error covariance operator is a gaussian filter and includes non-uniform and direction-dependent length scale
280 correlation radius to account for anisotropic coastal assimilation (Terruzzi et al., 2018) and vertical profile assimilation
281 (Cossarini et al., 2019). The vertical error covariance operator is based on a set of vertical error profiles obtained using an
282 empirical orthogonal functions (EOFs) decomposition of a pre-existing biogeochemical simulation. EOFs are computed
283 monthly for the 16 subregions and rescaled at each grid-point considering the ratio between observation and model variances
284 (Teruzzi et al., 2018). The biogeochemical error covariance operator is designed to preserve the ratios among phytoplankton
285 functional types and their internal carbon to nutrient quotas (Teruzzi et al., 2014) and supports monthly and spatial varying
286 covariances between dissolved inorganic nutrients (Teruzzi et al., 2021).

287   In the most recent configuration (Teruzzi et al., 2021, Cossarini et al., 2019), the assimilated biogeochemical observations are

288   satellite multi-sensor (MODIS, VIIRS and OLCI) surface chlorophyll data (Volpe et al., 2019) and quality-controlled Argo-

289   BGC nitrate and chlorophyll profiles (Schmechtig et al., 2018; Johnson et al., 2018).

290

291   **2.4 Systems evolutions**

292   The Mediterranean has been the site of major forecasting research activities since the late nineties (Pinardi and Woods, 2001,

293   Pinardi et al., 2003, Pinardi and Coppini, 2010). Before 2008, only the PHY and BIO components were present. The PHY

294   component was based on the Ocean PArallelise (OPA) code (Madec et al., 1998) with the highest available horizontal and

295   vertical resolution of 1/16º degrees (approx. 6.5 km) in horizontal and 72 vertical levels, with closed lateral boundaries, only

296   7 major rivers and implementing a weekly 3D-VAR assimilation scheme (Dobricic et al., 2007) assimilating temperature and

297   salinity vertical profiles, Sea Level Anomaly (SLA) along with track altimeter data, moreover a non-solar heat flux correction

298   was imposed through a nudging along the whole day with Sea Surface Temperature (SST) satellite gridded data.

299   A major upgrade of the PHY component was achieved in 2009 by implementing a version of the numerical model NEMOv3.1

300   including LOBC in the Atlantic Ocean (Oddo et al. 2009) and moving to a daily assimilation cycle. The first exchanges with

301   a wave model were implemented in 2010 when the PHY component was coupled hourly with WAM receiving the surface drag

302   coefficient to better represent the wind stress. In 2013 the whole operational modelling system was updated by implementing

303   an upgraded 2-way on-line coupled system based on NEMOv3.4 and WW3 (Clementi et al., 2017a) allowing for a more

304   consistent exchange between the two models. The following year the PHY general circulation module was improved by

305   accounting for the effect of atmospheric pressure effect (in addition to wind and buoyancy fluxes) and an explicit linear free

306   surface formulation using a time splitting scheme (Oddo et al., 2014), while the assimilation scheme was enhanced thanks to

307   the assimilation of Tailored Altimetry Products for Assimilation Systems (TAPAS) SLA data allowing for the application of

308   specific corrections of the altimetric original signal (Dobricic et al., 2012).

309   The PHY component delivered in 2015 included the nesting in the Atlantic Ocean through daily analysis and forecast fields

310   from the global system, while one year later the assimilation scheme was enhanced including the computation of monthly and

311   grid point EOFs and vertical observational errors varying with depth.

312   Another major PHY component evolution was achieved in 2017 when the resolution of the operational system was increased

313   to 1/24º degrees (approx. 4 km) horizontal and 141 vertical levels using the z-star vertical coordinate system, a non-linear free

314   surface formulation and the NEMOv3.6 version and 39 rivers were introduced. From year 2019 the Dardanelles Strait inflow

315   was set as a lateral open boundary condition (instead as a river runoff climatological input) allowing for a daily update of the

316   fluxes, and an improved nudging with the satellite sea surface temperature was included by correcting the heat fluxes only

317   close to midnight.

318   The WAV component was developed and released for the first time in 2017 based on WAM Cycle 4.5.4 providing on a daily

319   basis 5 days wave forecasts and simulations for the Mediterranean Sea at 1/24º horizontal resolution (Ravdas et al., 2018)

320   nested within a North Atlantic model at 1/6º resolution and forced with ECMWF 10m winds and PHY component surface

321   currents. In March 2018 the system was upgraded by incorporating the data assimilation component to utilise available track

322   SWH satellite observations from Sentinel-3A and Jason-3. In 2019, the wave model was upgraded to Cycle 4.6.2 and the

323   duration of the forecasts were extended to 10 days. Additionally, a limitation to the high frequency part of the wave spectrum

324   was applied while modifications from default values were introduced in the input source and dissipation functions: ZALP was

325   set to 0.011 and C_{DS} and δ became 1.33 and 0.5 respectively.

326   In 2009, the first pre-operational version of the BIO component featured early versions of OGSTM transport model and BFM

327   model (Lazzari et al., 2010). The spatial resolution was 1/8°, which required a subsampling of the PHY component fields from

328   the 1/16° resolution. The Atlantic boundary was closed with a nudging term for nutrients and the land nutrients input included

329   the three major Mediterranean rivers (i.e., Po, Rhone and Nile) and the Dardanelles was treated as a river. BFM used constant

330   daily averaged irradiance to force photosynthesis (Lazzari et al., 2010).

331   Horizontal resolution aligned with the physical model in 2013 and was refined to 1/24° in 2017. Full alignment between The

332   PHY and BIO components in terms of same horizontal and vertical resolutions, bathymetry, boundaries (number and position

333   of rivers) was introduced in 2018 and remained a standard that mitigates possible approximation errors related to the use of

334   daily eddy-resolving ocean general circulation model to force the transport of tracers (Salon et al., 2019). Additionally, nutrient

335   and carbon land input from 39 rivers were introduced in 2017, open boundary conditions at Dardanelles Strait in 2019 and in

336   the Atlantic Ocean in 2020 (Salon et al., 2019).

337   Since 2008, three major improvements of the BFM model included the addition of the carbonate system to predict alkalinity,

338   ocean acidity and CO2 air-sea exchanges in 2016 (Cossarini et al., 2015), the revision of nutrient formulation of phytoplankton

339   in 2018 (Lazzari et al., 2016) and, in 2020, the introduction of the day-night cycle in light-dependent formulation of

340   phytoplankton (Salon et al., 2019) and of the novel light extinction coefficient (Terzic et al., 2021).

341   A major system evolution and quality improvement was achieved in 2013 with the inclusion of the assimilation of satellite

342   chlorophyll through a variational scheme with prescribed background error covariance (Teruzzi et al., 2014). Assimilation

343   method was improved in 2018 to include coastal component (i.e., non-uniform and direction-dependent horizontal covariance;

344   Terruzzi et al., 2018) and in 2019 to integrate new observations (i.e., Argo-BGC float profiles) including new parameterization

345   for the vertical and biogeochemical background error covariance (Cossarini et al., 2019).

346   In terms of operational product delivery, the BIO component has produced daily 10-day forecasts and weekly 7-day analysis

347   since 2020, fully aligned with the PHY component (Salon et al., 2019). Before that, the system produced 7-day analysis and a

348   7-day forecast once per week since 2013, while a second cycle of 7-day forecasts was added each week in 2015.

3. Quality assessment

The evaluation of the quality of the Med-MFC is given here only for the analysis products, leaving the assessment of the forecast skill for future work. One overarching driver for the Med-MFC evolution is the continuous improvement of the numerical model and data assimilation modules with respect to a well-defined set of goodness indices established for all the European regional Seas (Hernandez et al., 2009).

3.1. PHY component skill

The skill of the physical analysis fields is assessed over a 3 years period from 2018 to 2020 comparing model results (Clementi et al., 2019) to satellite and in-situ observational datasets by means of root mean square differences (RMSD) and bias (model minus observations) of daily mean analysis outputs, so called Estimated Accuracy Number (EAN) and misfits, calculated at observation time during the forward model integration and evaluated on a sub-set of observations corresponding to the ones assimilated by the system. In EAN, the daily mean analyses are interpolated on daily available observations: this goodness score is somewhat approximated especially at the surface where daily variability is large, but this is a score used by many forecasting systems (Ciliberti et al., 2022; Toledano et al., 2022; Sotillo et al., 2021, Najy et al., 2020) and we will show it for reference purposes.

Table 2 summarises the EAN of 3D model temperature and salinity daily mean values compared to in situ observations, in particular Argo floats and CTD profiles average over the three reference years. Model temperature is generally warmer than observations, i.e., it shows a positive bias, with the largest error (maximum value of the period is 0.8°C) in the sub-surface layers between 10 and 60 m, decreasing with depth. Salinity is characterised by a negative bias, meaning generally lower salinities than measured, along the whole water column. The salinity RMSD yearly mean values is lower than 0.22 PSU, the error is larger in the first layers and decreases significantly below 150 m. The comparison with other Copernicus Marine Service forecasting systems EAN values presented in the Quality Information Document (QUID) considering that the validation periods are different, shows that the Mediterranean temperature and salinity quality in terms of RMSD are aligned with all the other Copernicus forecasting systems. In particular the SST averaged RMSD with respect to satellite data ranges from 0.48°C in the North West Shelf (derived from the QUID of the product NORTHWESTSHELF_ANALYSIS_FORECAST_PHY_004_013 https://doi.org/10.48670/moi-00054) to 0.8°C in the Baltic Sea (derived from the QUID of the product BALTICSEA_ANALYSISFORECAST_PHY_003_006 https://doi.org/10.48670/moi-00010), while the 3D mean temperature RMSD with respect to *in-situ* data ranges from 0.4°C in the Mediterranean and North West Shelf to 0.7°C in the Black Sea (derived from the QUID of the product BLKSEA ANALYSISFORECAST_PHY_007_001 https://doi.org/10.25423/cmcc/blksea_analysisforecast_phy_007_001_eas4) and the salinity mean RMSD varies from 0.1PSU in the Mediterranean and North West Shelf to 0.3PSU in the Iberia-Biscay-Ireland area (derived from the QUID of the product IBI_ANALYSISFORECAST_PHY_005_001 https://doi.org/10.48670/moi-00027). The sea level anomaly skill is also aligned with the ones of other operational systems within the Copernicus Marine

381   Service when compared with satellite altimeter observations (from 2.2cm in the Black Sea to 9cm in the North West Shelf

382   area).

383   The other goodness index is computed as weekly mean root mean square error and bias using temperature and salinity misfits,

384   that are computed at FGAT. The misfits are more precise to account for surface errors since the observations are compared

385   with the model at the exact time of the day when observations are taken. This index is represented as a depth-time Hovmoller

386   diagram in Figure 4. The temperature error is seasonal (Figure 4a), with maximum values of ~1.8ºC in the range of 30-60 m

387   depth corresponding to the depth of the mixed layer and the seasonal thermocline during the stratified season, from June to

388   November. The error is reduced to an average value of around 0.4ºC during the vertically mixed season from December to

389   May. The temperature bias (Figure 4c), as already shown in Table 2 for EAN, indicates an overall overestimation of the

390   temperature except for the subsurface during winter and spring. The positive bias could be caused by an overestimation of the

391   downward shortwave radiation flux which is estimated according to Reed (1977) formula, as already discussed in (Byun et al.,

392   2007) and (Pettenuzzo et al., 2010).

393   The salinity error (Figure 4b) is defined by two main structures: one that is constant throughout the year down to about 150 m

394   and the seasonal amplification during summer, as for the temperature errors. The maximum errors reach values of 0.35 PSU

395   in the summer period and decrease to 0.025 PSU below ~150 m. We argue that the background error, uniform throughout the

396   year, could be due to inaccurate advection of salinity in different sub-areas of the Mediterranean Sea. Moreover, the model

397   salinity bias is negative, i.e., the model salinity is lower than the observations (Figure 4d). This could be related to the larger

398   Atlantic water inflow with respect to literature (Soto-Navaro et al., 2010) at Gibraltar as reported in Table 3 and to inaccurate

399   mixing at Gibraltar due to the lack of tides.

400   Sea surface temperature (SST) and sea level anomaly (SLA) skills are evaluated comparing them with satellite observations:

401   model daily mean SST is compared to SST satellite L4 gridded data at 1/16° resolution (Buongiorno Nardelli et al., 2018)

402   while SLA is compared to along with track satellite altimeter observations (Taburet et al., 2019) in terms of model misfits.

403   Table 4 presents the EAN RMSD values computed for SST and misfit SLA RMSD averaged in the Mediterranean Sea and

404   over the 16 sub-regions, presented in Figure 3. Considering SST, the EAN RMSD values range between 0.47 °C and 0.69°C

405   (mean Mediterranean Sea error of 0.54 °C), while the SLA error ranges between 2.3 cm and 5.3 cm (mean error is 3.8 cm).

406   The quality of the analysis varies in different regions depending on the spatial distribution of the observations (for SLA) in

407   addition to the model inaccuracies.

408   The time variability of the model SLA accuracy is also provided by means of weekly model misfits evaluated for each available

409   satellite altimeter and averaged in the whole Mediterranean Sea as shown in Figure 5. The error ranges between 2.5 cm and

410   5.5 cm (maximum error with respect to Cryosat) with a large variability among the different satellites, with a generalised

411   increase of error during Autumn and Winter seasons.

3.2. WAV component skill

The quality of the wave analysis and forecast product is assessed over a three-year period from January 2018 to December 2020. Model analysis and first-guess (i.e. just before data assimilation) outputs are compared to in-situ and satellite observations respectively.

Significant wave height (SWH) and mean wave period (MWP) measurements are used for data validation from 28 wave buoys in the Mediterranean Sea (Figure 6 lower panel). Data quality control procedures have been applied to the in-situ observations (Copernicus Marine In-Situ Team, 2020) and measurements associated with a bad quality flag are not taken into consideration. Figure 6 depicts scatter plots of the evaluation of the observed SWH and MWP against measurements, obtained from the 28 buoys. The figure reveals small SWH underestimation by the model mainly for very small wave heights (< 0.6 m). A prevalence of model overestimation is obtained for waves above about 2m, which becomes more pronounced for higher waves. Regarding MWP, the model underestimates the observations for MWP < 7 s whilst model overestimation is observed for higher periods. Equivalent seasonal results (not shown) revealed that the performance of the model is better in winter than in summer which agrees with other studies (Cavaleri and Sclavo, 2006; Ravdas et al., 2018).

The qualification metrics for the different buoy locations in Fig. 6 is plotted in Figure 7 (upper panel). RMSD at the different buoy locations varies from 0.13 m to 0.31 m. Scatter Index (SI) varies from 0.17 at buoy 3732621 to 0.35 at the buoys of Malaga and SARON (Aegean Sea). In general, SI values above the mean value for the whole Mediterranean Sea (0.24) are obtained at wave buoys located near the coast, particularly if these are sheltered by land masses on their north-northwest (e.g. western French coastline), and/or within enclosed basins characterised by a complex topography such as the Aegean Sea. As explained in several studies (Ravdas et al., 2018), in these cases, the spatial resolution of the wave model is often not adequate to resolve the fine bathymetric features whilst the spatial resolution of the forcing wind model is incapable to reproduce the fine orographic effects, introducing errors to the wave analysis. The Correlation coefficient (CORR) mostly follows the pattern of variation of the SI. It ranges from 0.87 at SARON in the Aegean Sea to 0.97 at the deep-water buoy 6100196 offshore Spain, which is well exposed to the prevailing north-westerly winds in the region. The BIAS varies from -0.13 m at buoy 3732621 (located north of Crete) to 0.13 at buoy 6100021 located near the French coast. Its sign varies, with positive and negative values computed at almost the same number of locations respectively. Overestimation at buoy 6100198 in the Alboran Sea is part of a general overestimation of the wave heights in the Atlantic and Alboran regions as will be seen later in the comparison with satellite observations.

Figure 8 (right) shows the scatter plot between the first guess SWH and satellite observations. Here the initial guess SWH refers to the model SWH before data assimilation, thus meaning semi-independent model data. In addition, a scatter plot resulting from the comparison of the ECMWF forcing wind speeds (U10) and satellite measurements of U10 is shown in Figure 8 (left). It is seen that ECMWF is forcing underestimates observed U10 throughout the entire U10 range, even more so at high wind speeds. An overall ECMWF overestimation of 3% is computed. On the other hand, the SWH model underestimation is about 6%. The model underestimates SWH for the lower range (< 2.5 m) and overestimates SWH for larger

445   waves. Compared to the equivalent results obtained from the model-buoy comparison, a smaller scatter (by about 7%) with a

446   larger overall bias is associated with the model-satellite comparison, i.e. open ocean waves. SI values compare well at the more

447   exposed wave buoys in the Mediterranean Sea.

448   Figure 9 maps statistics of the comparison of model first-guess and satellite observations of SWH for the different sub-regions

449   of the Mediterranean Sea. The Aegean and Alboran Seas have relatively high SI values (0.21). The highest value of SI is

450   obtained for the North Adriatic Sea (0.26) followed by the South Adriatic (0.23). The lowest values (0.13-0.15) are found in

451   the Levantine Basin, the Ionian Sea, and the Southwest Mediterranean Sea. Relatively low values (0.16) are also found west

452   of the islands of Sardinia and Corsica. As discussed above, the error is due to inaccuracies associated with orographic winds

453   and/or local sea breezes and the missing representation of the complicated bathymetry in the fetch-limited, enclosed regions.

454   SWH negative bias is present in all sub-regions.

455   Finally, inter-compared to ECMWF, UK MetOffice and DMI (Danish Meteorological Institute) wave forecasting systems for

456   a different year (2014), Med-waves shows a better skill in terms of SWH with RMS errors for the Western Med buoys equal

457   to 0.227 m (0.234m for ECMWF; 0.281 for UK MetOffice) and 0.201m for the central and eastern Mediterranean (0.227m for

458   ECMWF; 0.268 for DMI).

459

460   **3.3. BIO component skill**

461   The BIO component state variables can be validated at three different uncertainty levels providing a "degree of confirmation"

462   (Oreskes et al., 1994) of different scales of variability based on the availability of reference data.

463   Near real time satellite and Argo float data provide a rigorous skill performance validation data set down to the scales of the

464   week and mesoscale dynamics for a limited set of variables: chlorophyll, nitrate and oxygen. Dataset of historical

465   oceanographic data (Socat dataset, Baker et al (2016); EMODnet data collection, Buga et al. (2018), Cossarini et al., (2017);

466   Lazzari et al., (2016)) are used to build a reference framework of sub-regions and annual and seasonal climatological profiles

467   to validate model performance to simulate the basin wide gradients, the mean vertical profiles and the seasonal cycle. For this

468   data set it is possible to have nutrients, such as nitrate, phosphate, ammonia and silicate, as well as dissolved oxygen, dissolved

469   inorganic carbon, alkalinity and surface pCO2.

470   Lastly, a third level of validation regards those variables whose observability level is very scarce (e.g., phytoplankton biomass)

471   or based on indirect estimations (e.g., primary production, air-sea CO2 fluxes). Only confirmation of the range of variability

472   and a general uncertainty estimation can be provided for those variables (see for example the validation of model primary

473   production in (von Schuckmann et al., 2020; Cossarini et al., 2020).

474   Considering the 2018-2020 reference period, the chlorophyll is very well reproduced by the BIO component, both in terms of

475   seasonal cycle and spatial gradient at surface (Figure 10) and in terms of vertical profiles at the Argo float positions (Table 5).

476   Uncertainty of surface chlorophyll is lower than 0.03 mmol/m3 with larger values registered in winter and western sub-regions

477   where the variability and the chlorophyll values are higher (Figure 10a and b). Regarding profiles, chlorophyll values and

478 vertical shapes driven by mesoscale dynamics are simulated with a high level of accuracy by the model (Salon et al., 2019;
479 Cossarini et al., 2019, 2021). Indeed, (Salon et al., 2019) show how, using novel metrics, the BIO component reproduces with
480 high level of accuracy not only the concentrations in the euphotic layer, but also the seasonal evolution of the shape of the
481 profiles. The depth of the deep chlorophyll maximum during summer and of the surface bloom during winter, as well as the
482 depth of the nitracline and the depth of the maximum oxygen layer, which results from the interaction of physical and
483 biogeochemical processes, are reproduced with an uncertainty of the order of a meter (Table 5). However, the conclusions
484 about mesoscale accuracy of the BIO component should be taken with caution since the observations are still relatively few in
485 number (about 1 over 8 w.r.t. the Argo floats have biochemical sensors) and unevenly spaced (e.g., southern Mediterranean
486 Sea is less observed than northern areas).

487 As explained above, an additional verification of biogeochemical variables can be achieved for additionally 7 variables (not
488 considering chlorophyll) and two other derived variables with climatological data. An example of such comparison is shown
489 in Figure 11 for the carbonate system variables. Average maps and profiles of Alkalinity and DIC in selected sub-regions in
490 the zonal directions (coloured lines) are well superimposed to the range of variability of the historical in-situ data (grey shaded
491 areas) demonstrating the capability of the BIO component to reproduce both horizontal basin-wide gradients and vertical
492 profiles in the different areas.

493 As a summary of the skill performance analysis, statistics based on RMSD for all the considered model variables (Table 6)
494 reports the model uncertainty in reproducing the basin-wide values and gradients for the selected layers. Generally, larger
495 errors are computed for the upper layers where the variability (both spatial and temporal) is higher. Ammonia reports high
496 errors also in subsurface layers, which is due to a possible incorrect initialization of deep layers since the lack of data in 9 out
497 of 16 sub-regions. These numbers, which respond to the request for a synthetic measurement of Copernicus Marine Service
498 product accuracy (Hernandez et al., 2018), are consolidated by in deep skill performance analysis of BFM model in reproducing
499 chlorophyll (Lazzari et al., 2012; Teruzzi et al., 2018), nutrients (Lazzari et al., 2016, Salon et al., 2019) and carbonate system
500 variables (Cossarini et al., 2015).

501 Chlorophyll from Ocean Color is the most common variable used for validation and near real time assessment of operational
502 biogeochemical models and allows for a comparison of the forecast skill performance among the Marine Copernicus systems.
503 Results of surface chlorophyll skill scores show that the quality of the first day of forecast of the BIO component is in line
504 with those of other Copernicus models[1] (Spruch et al 2020; Vandenbulcke et al 2022; McEwan et al, 2021; McGovern et al
505 2020). In particular, the two proposed accuracy indexes (i.e., one minus scatter index and one minus the root mean square error
506 normalised on variability) of the MED model equal to 34% and 47%, which are within the ranges of the other Copernicus
507 systems: 11%-38% and 13%-73% for the two skill scores, respectively (Spruch et al 2020; Vandenbulcke et al 2022; McEwan
508 et al, 2021; McGovern et al 2020).

---

[1] Product Quality Dashboard, Green Ocean section, https://pqd.mercator-ocean.fr/, accessed 15 July 2022.

509 For other biogeochemical variables, a direct comparison of the accuracy among Copernicus models is not straightforward,

510 given the different protocols for metrics computation, the representativeness of the available observations and the large range

511 of variability of observed values of biogeochemical variables among the European seas. Nevertheless, a rough comparative

512 assessment of the quality of Marine Copernicus biogeochemical models can be provided using published estimated accuracy

513 numbers (EANs) and the typical values of the variables (McEwan et al., 2021; Feudale et al., 2021; Spruch et al., 2020; Melsom

514 and Yumruktepe, 2021; McGovern et al., 2020; Vandenbulcke et al., 2021) to derive a common index of relative uncertainty.

515 As for examples, relative uncertainty of oxygen of the MED system is of the order of 2% which is in line with the other

516 Copernicus systems, except for Baltic and Black Seas systems, which show slightly higher relative errors. For nutrients, nitrate

517 and phosphate uncertainties of the MED are about 50% and 35% which are similar or slightly better than most of the other

518 Copernicus marine biogeochemical systems (i.e., ranges of 30-75% and 30-50% for nitrate and phosphate, respectively).

519 Finally, the relative uncertainty of pH simulated by the MED system is less than 0.5% while other Copernicus systems report

520 relative errors of the order of 1-2%.

521 Beside the aforementioned comparison, it is worth to report that the MED biogeochemical system exhibits some

522 distinguishable features: the continuous monitoring of the forecast skill of surface chlorophyll since the beginning of the

523 operational biogeochemical system dating back to 2010 (Salon et al., 2019), a large number of validated variables with in-situ

524 data (i.e., up to 10 variables, Table 6), the thorough use of Argo-BGC observations for near real time validation (Salon et al.,

525 2019, Cossarini et al., 2021; https://medeaf.ogs.it/nrt-validation, last visit August 2022).

526 **4. Conclusions and Future Perspectives**

527 In this paper, the Med-MFC components, PHY, BIO and Wav have been described providing an overview of their technical

528 specifications. The system is offline coupled and the PHY component exchanges 3D currents, temperature, salinity with the

529 BIO and WAC components daily, with daily mean values. This approximation is flexible enough that improvements can be

530 carried out separately on the three components, considering different levels of maturity of the numerical modelling

531 parametrizations, the data assimilation components and the validation data sets. Three different data assimilation system are

532 run for each component making the best use of all available data from satellite and in-situ, the effort is to assimilate as much

533 data as possible and use background or model uncertainties to account for the missing couplings. The 3 components accuracy

534 has been evaluated for a common three-year period, from Jan 2018 to Dec. 2020.

535 The PHY component shows a warm bias at surface of +0.7°C compared to satellite SST. The RMSD has a clear seasonal

536 signal with the largest errors due to the depth of the surface mixed layer and the seasonal thermocline. The model salinity is

537 higher in the first layers and decreases significantly below 150 m. The analysis SLA presents an average error of 3.8cm on a

538 three-year average.

539 The WAV component was extensively validated for the 3-year period using all available in-situ and satellite observations in

540 the Mediterranean Sea. All statistical values calculated and presented here showed a very good system performance. It is

541 concluded that the Mediterranean SWH is accurately simulated by the WAV component. The typical SWH difference with

542 observations (RMSE) over the whole basin is 0.21 m (0.202 m for in-situ and 0.214 for satellite observations) with a bias

543 ranging from -0.004 m, when the comparison is against the in-situ observations, to -0.0031 m when the comparison is with

544 satellites. The scatter index (SI) exhibits low values (15%-17%) over the majority of the basin and relatively higher values

545 (21%-22%) over the Aegean, Alboran, Ligurian and South Adriatic Seas (highest SI equal to 28% occurs in the North Adriatic).

546 As explained, the occurrence of higher SI values is mainly related to the quality of ECMWF winds in fetch-limited areas of

547 the basin where the orographic effects play an important role and the difficulties of wave models to appropriately resolve

548 complicated bathymetry and coastline.

549 Overall, the quality of the WAV component stems out of the weakly coupled offline coupling between PHY and WAV. In

550 particular, the WAV component assimilates data with a well calibrated stand-alone OI scheme using satellite altimetry data

551 and implements regular updates and improved parameterization independently from the other components.

552 The BIO system has defined a validation framework (Salon et al., 2019) based on the near real time observations (i.e., satellite

553 and Argo) showing average errors in the 0-200m layer of 0.04 mg/m3, 0.4 mmol/m3 and 16.8 mmol/m3 for chlorophyll, nitrate

554 and oxygen, respectively.

555 Since 2008 the Med-MFC components have been continuously upgraded and substantially improved. The system evolution

556 will continue also in the future following the main drivers of the three components, the Copernicus Marine Service users.

557 Considering the PHY component, the user needs finer spatial scales and higher time frequencies of the products. User require

558 also higher accuracy in storm surge forecasting including tidal forcing and improved representation of lateral open boundary

559 conditions (e.g., rivers, nesting in the Atlantic and the Black Sea). The Med-MFC offers a unique opportunity to model the

560 coastal areas at the resolution of few hundred meters using nesting schemes (Federico et al., 2017, Trotta et al. 2021). Finally,

561 the future should consider ensemble forecasting to recast the deterministic forecast in within a probabilistic framework (Pinardi

562 et al, 2011, Millif et al, 2009, Thoppil et al, 2021; Barton et al., 2021). Another important goal for the future is to assimilate

563 Argo and drifter trajectories (Nelson et al., 2016) and gliders (Dobrici et al., 2009) as well as tidal coastal station at sea level.

564 User needs for the future evolution of the WAV component indicate the increase of the frequency of the wave analyses, making

565 available larger data sets such as the wave spectra and dedicated products (like the directional spread at peak frequency and

566 different parts of the wave spectrum). Extreme waves forecasting requires also a probabilistic approach. The required increased

567 accuracy can be achieved by improving the quality of the wind forcing using downscaled ECMWF forecasts and assimilating

568 additional satellite (wave spectrum from SAR) or higher frequency in-situ wave measurements. Also, for the WAV component,

569 the development of a WAB ensemble prediction system will be necessary.

570 In the light of the user needs and requirements, the BIO component validation framework helped to identify strengths and

571 weaknesses of the model system for future developments. In the BIO component case, future upgrades should be related to the

572 development of the BFM biogeochemical model process representations and model parameter estimation. This includes

573 increasing the number of phytoplankton functional types and zooplankton compartments to describe diversity of the plankton

574 community and the different energy and matter pathways across the ecosystem. Additionally, the integration of optics and

575 biogeochemistry including new coupled modelling and novel hyperspectral and high-resolution radiometric data will be

576 beneficial for calibrating parameters of key ecosystem processes (Lazzari et al., 2021).

577 Regarding the BIO component assimilation framework, the future developments should consider the assimilation of

578 biochemical variables from new sensors such as novel satellite and in situ Argo and Gliders (Cossarini et al., 2019) and the

579 evolution of the 3DVarBio towards hybrid-3Dvar or ensemble-3Dvar methods (Carrassi et al., 2018) and joint physical-

580 biogeochemical data assimilation.

581

582

583 **Author Contributions:** G.C. (Coppini) and E.C. coordinated the preparation of the paper in collaboration with G.C. (Cossarini), and G.K.

584 E.C., G.C. (Cossarini) G.K., P.L., A.T., G.B., J.P, A.C.G., A.A., R.E., A.C., D.D., S.M., A.N., N.P., M.R. contributed to the system and
585 models development; V.L., A.G., L.F., C.A., V.D., A.M., A.C.G, A.Z., C.O., E.C. contributed to the model validation and assessment; R.L.,
586 M.D., A.M., A.B., GL.C., contributed to the operational activities. All authors contributed to the final version of the paper.

587 **Funding:** This work has been funded through the EU Copernicus Marine Med-MFC Service Contact n.74.

588 **Acknowledgments:** This study has been conducted using EU Copernicus Marine Service Information. Within the Copernicus Marine
589 Service of the MED-MFC CMCC is in charge of the coordination of the service and responsible for the Physics (ocean circulation)
590 Production Unit, OGS is responsible for the BIO (biogeochemical) Production Unit and HCMR is responsible for the WAVE Production
591 Unit. The authors thank CINECA (Italian supercomputer centre) for the technical support provided in the biogeochemical component
592 production workflow.

593 **Conflicts of Interest:** The authors declare no conflict of interest

594

595

Appendix A

597

Table A1. List of the NEMO and WW3 numerical setup for the PHY component

599

Parameter	Value
NEMO model version	3.6
Horiz. Resolution	1/24°
Vertical discretization	141 z levels with partial cells
Vertical coordinates	zstar
Time-step	240 s
Number of barotropic iterations	100
Free-surface formulation	Non-Linear free surface with split-explicit free surface
Air-sea fluxes	MFS-Bulk formulae
Atmospheric Pressure	Yes
Wave coupling	Neutral drag coefficient
Runoff	Surface boundary condition with specific treatment at river mouth and prescribed river salinity
Sea Surface Restoring T/S	only for temperature
Solar radiation penetration	2-band exponential penetration (insert the decay length and the transmission coeff)
Lateral momentum B.C.	No-slip
Lateral Open B.C.	Flather open boundary condition for barotropic currents, Orlansky for total currents and tracers
Bottom B.C	Non-linear friction with logarithmic formulation

Equation of State	EOS-80
Tracer Advection	Up-stream/MUSCL
Tracers Horiz. Diffusivity	Bi-Laplacian coeff = -1.2.e8 [m4/s]
Momentum Horiz. Viscosity	Bi-Laplacian coeff = -2e.8 [m4/s]
Momentum Advection	Vector form (energy and enstrophy cons. scheme)
Turbulent vertical viscosity scheme	Richardson number dependent formulation following Pacanowsky Philander (1981) and Lermousiaux (2001) adjustment
Background Vertical Visc.	1.2e-6 [m2/s]
Background Vertical Diff.	1.0e-7 [m2/s]
Vertical time stepping scheme	Implicit
WW3 model version	3.14
Horiz. Resolution	1/24o
Number of frequencies	30
Number of directions	24
Time-step (global)	240 s
Wind input term	Janssen's quasi-linear theory (Jansen, 1989; Jansen, 1991)
Wave dissipation term	Hasselmann (1974) according to Komen et al., (1984)
Non-linear wave-wave interaction term	Discrete Interaction Approximation (DIA, Hasselmann et al., 1985)
Coupling with NEMO	Sea surface currents, sea surface temperature

600

601

602   **Table A2.** List of the WAM model set up for the WAV component.

Parameter	Value

WAM model version	Cycle 4.6.2
Horiz. Resolution	1/24°
Geographical domain	18.125°W - 36.2917°E 30.1875°N - 45.9792°N.
Depth map	GEBCO 30arc-second
Number of frequencies	32
Number of directions	24
Time-step (propagation)	60 s
Time-step (sources)	360 s
Deep/Shallow mode	Shallow
10m winds	ECMWF 10m analyses and forecast winds
C_{DS}, δ	1.33, 0.5
ZALP	0.011
Surface currents coupling	Offline coupled with Med-MFC NRT daily surface currents
Data assimilation	Optimal Interpolation method / Altimeter satellite data provided by Copernicus Marine Service are assimilated in the wave model.

603

604

605

606 **Table A3.** List of the OGSTM-BFM model set up for the BIO component.

Parameter	Value
OGSTM model version	4.1
BFM model version	5.0
3DVarBio version	3.3
Horiz. Resolution	1/24o
Geographical domain	9.0°W - 36.2917°E 30.1875°N - 45.9792°N.
OGSTM: physical forcing	U, V, W, eddy diffusivity, SSH
OGSTM: timestep	450 s
OGSTM: off-line coupling frequency	1 d
OGSTM: advection scheme	Smolarkiewicz
OGSTM: horizontal diffusion	Bi-Laplacian coefficient -3.e9 [m4/s]
OGSTM: vertical diffusion scheme	implicit 2nd order
BFM parameters for Phytoplankton, Zooplankton, Bacteria, DOM and POM formulation	as in (Lazzari et al., 2012) and 2016
BFM light: type of model	instantaneous light from short wave radiation, light at the centre of the grid cell
BFM light: Fraction of Photosynthetically Available Radiation	0.40
BFM light: conversion W/m2 to moli quanta/m2/s	1./0.217 Watt / umol photons
BFM light: background extinction coeff.	0.0435 1/m
BFM light: specific attenuation coefficient of particulate	0.001 m2/mgC

BFM carbonate system: solver using total alkalinity and DIC	SolveSAPHE v1.0.1 routines (Munhoven, 2013)
BFM carbonate system: K0, solubility of co2 in the water (K Henry)	Weiss 1974
BFM carbonate system: k1 and k2 constants for carbonic acid	Mehrbach et al. (1973) refit, by Lueker et al. (2000) (total scale)
BFM carbonate system: Kb constant for boric acid	Millero p.669 (1995) using data from Dickson (1990) (total scale)
BFM carbonate system: k1p, k2p and k3p constants of phosphoric acid	Millero (1974)
BFM carbonate system: Ksi constant of orthosilicic acid	Millero (1995)
BFM carbonate system: Kw of water dissociation	Millero (1995)
BFM carbonate system: ks of sulfuric acid	Dickson (1990)
BFM carbonate system: kf of folic acid	Perez & Fraga (1987) recom. by Dickson et al., (2007)
BFM carbonate system: air-sea exchange model	Wannikoff et al., 2014
3DVarBio: max depth of assimilation	200m
3DVarBio: n. of vertical EOFs	26
3DVarBio: horizontal correlation radius	variable in X and Y; average 15 km (Teruzzi et al., 2018)
3DVarBio: solver for cost function J	quasi-Newton L-BFGS minimizer
3DVarBio: Minimum gradient of J	1.0E-11
3DVarBio: Percentage of initial gradient	0.01
3DVarBio: n. of interactions of recursive filter	4

607
608
609
610

611   **Table A.4.** River sources implemented as freshwater inputs in the physical and biogeochemical models, including river name, the annual
612   mean runoff and the imposed salinity at river mouth.

613
614

River Name	Mean annual Runoff [m3/s]	Salinity at river mouth [psu]
Ebro	432	30
Rhone	1707	25
Po	1519	18
Buna-Bojana	675	15
Seman	201	15
Vjosa	183	15
Nile	475	8
Aude	59	15
Arno	88	15
Tevere	181	15
Volturno	63	15
Medjerda	59	15
Reno	67	15
Adige	232	15
Brenta	163	15
Piave	129	15
Livenza	96	15
Tagliamento	79	15
Isonzo	175	15
Lika	84	15
Krka	57	15
Neretva	239	15
Trebisnjica	93	15
Mati	99	15
Shkumbini	54	15
Arachtos	75	15
Acheloos	106	15
Pineios	67	15
Axios	97	15
Struma	81	15
Maritza	166	15
Gediz	53	15
Buyuk Menderes	106	15
Köprüçay/Eurimedonte	85	15
Manavgat	122	15
Goksu	203	15
Seyhan	200	15

Ceyhan	231	15
Orontes	94	15

615
616

References

Adani, M., Dobricic, S., Pinardi N.: Quality Assessment of a 1985–2007 Mediterranean Sea Reanalysis. J. Atmos. Oceanic Technol., 28, 569–589., doi:10.1175/2010JTECHO798.1, 2011.

Alves, J.-H.G.M.: Numerical modeling of ocean swell contributions to the global wind-wave climate. Ocean Model, 11, 98–122. doi:10.1016/j.ocemod.2004.11.007, 2006.

Álvarez, M., Sanleón-Bartolomé, H., Tanhua, T., Mintrop, L., Luchetta, A., Cantoni, C., et al.: The CO_2 system in the Mediterranean Sea: a basin wide perspective. Ocean Sci. 10, 69–92. doi: 10.5194/os-10-69-2014, 2014.

Ayoub, N., Le Traon, P.-Y., De Mey: P. A description of the Mediterranean surface variable circulation from combined ERS-1 and Topex/Poseidon altimetric data. J. of Mar. Syst. 18 (1–3), 3–40, 1998.

Bakker, D. C. E., Pfeil, B., Smith, K., Hankin, S., Olsen, A., Alin, S. R., Cosca, C., Harasawa, S., Kozyr, A., Nojiri, Y., O'Brien, K. M., Schuster, U., Telszewski, M., Tilbrook, B., Wada, C., Akl, J., Barbero, L., Bates, N. R., Boutin, J., Bozec, Y., Cai, W.-J., Castle, R. D., Chavez, F. P., Chen, L., Chierici, M., Currie, K., De Baar, H. J. W., Evans, W., Feely, R. A., Fransson, A., Gao, Z., Hales, B., Hardman-Mountford, N. J., Hoppema, M., Huang, W.-J., Hunt, C. W., Huss, B., Ichikawa, T., Johannessen, T., Jones, E. M., Jones, S., Jutterstrøm, S., Kitidis, V., Körtzinger, A., Landschützer, P., Lauvset, S. K., Lefèvre, N., Manke, A. B., Mathis, J. T., Merlivat, L., Metzl, N., Murata, A., Newberger, T., Omar, A. M., Ono, T., Park, G.-H., Paterson, K., Pierrot, D., Ríos, A. F., Sabine, C. L., Saito, S., Salisbury, J., Sarma, V. V. S. S., Schlitzer, R., Sieger, R., Skjelvan, I., Steinhoff, T., Sullivan, K. F., Sun, H., Sutton, A. J., Suzuki, T., Sweeney, C., Takahashi, T., Tjiputra, J., Tsurushima, N., Van Heuven, S. M. A. C., Vandemark, D., Vlahos, P., Wallace, D. W. R., Wanninkhof, R. and Watson, A. J.: An update to the Surface Ocean CO_2 Atlas (SOCAT version 2), Earth Syst. Sci. Data, 6, 69-90, doi:10.5194/essd-6-69-2014, 2014.

Barton N.,E. Metzger J., C. A. Reynolds, B. Ruston, C. Rowley, O. M. Smedstad, J. A. Ridout, A. Wallcraft, S. Frolov, P. Hogan, M. A. Janiga, J. F. Shriver, J. McLay, P. Thoppil, A. Huang, W. Crawford, T. Whitcomb, C. H. Bishop, L. Zamudio, M. Phelps: The Navy's Earth System Prediction Capability: A new global coupled atmosphere-ocean-sea ice prediction system designed for daily to subseasonal forecasting. Earth Space Sci. 8, e2020EA001199, 2021.

Bergamasco, A., Malanotte-Rizzoli, P.: The circulation of the Mediterranean Sea: a historical review of experimental investigations, Adv. Oceanogr. Limnol, 1:1, 11-28, DOI: 10.1080/19475721.2010.491656, 2010.

Brassington, G. B.: Forecast Errors, Goodness, and Verification in Ocean Forecasting. Journal of Marine Research, Volume 75, Number 3, pp. 403-433(31). https://doi.org/10.1357/0022240017821836851, 2017.

Byun, D. S., Pinardi, N.: Comparison of Marine Insolation Estimating methods in the Adriatic Sea, Ocean Sci. J. 42(4), 211–222, 2007.

Buongiorno Nardelli, B., Tronconi, C., Pisano, A., Santoleri, R.: High and Ultra-High resolution processing of satellite Sea Surface Temperature data over Southern European Seas in the framework of MyOcean project, Rem. Sens. Env., 129, 1-16, doi:10.1016/j.rse.2012.10.012, 2013.

Buga, L., Sarbu, G., Fryberg, L., Magnus, W., Wesslander, K., Gatti, J., Leroy, D., Iona, S., Larsen, M., Koefoed Rømer, J., Østrem, A.K., Lipizer, M., Giorgietti, A: Data from: EMODnet Chemistry Eutrophication and Acidity aggregated datasets v2018. https://doi.org/10.6092/EC8207EF-ED81-4EE5-BF48-E26FF16BF02E, 2018.

Canu, D., Ghermandi, A., Nunes, P., Lazzari, P., Cossarini, G., Solidoro, C.: Estimating the value of carbon sequestration ecosystem services in the Mediterranean Sea: An ecological economics approach. Global Environmental Change. 32. 10.1016/j.gloenvcha.2015.02.008, 2015.

668 Carrassi, A., Bocquet, M., Bertino, L., Evensen, G.: Data assimilation in the geosciences: An overview of methods, issues, and
669 perspectives. Wiley Interdisciplinary Reviews: Climate Change, 9(5), e535, 2018.

671 Cavaleri, L., Sclavo, M.: The calibration of wind and wave model data in the Mediterranean Sea. Coast. Eng. 53, 613–627,
672 2006.

674 Cessi, P., Pinardi, N., Lyubartsev, V,: Energetics of Semienclosed Basins with Two-Layer Flows at the Strait. J. Phys.
675 Oceanogr., 44, 967–979. doi: 10.1175/JPO-D-13-0129.1, 2014.

677 Ciliberti, S.A., Jansen, E., Coppini, G., Peneva, E., Azevedo, D., Causio, S., Stefanizzi, L., Cretì, S., Lecci, R., Lima, L.,
678 Ilicak, M., Pinardi, N., Palazov, A.: The Black Sea Physics Analysis and Forecasting System within the Framework of the
679 Copernicus Marine Service. J. Mar. Sci. Eng., 10, 48. https://doi.org/10.3390/jmse10010048, 2022.

681 Clementi, E., Oddo, P., Drudi, M., Pinardi, N., Korres, G., Grandi, A.: Coupling hydrodynamic and wave models: first step
682 and sensitivity experiments in the Mediterranean Sea. Oc. Dyn., doi: https://doi.org/10.1007/s10236-017-1087-7, 2017a.

684 Clementi, E., Pistoia, J., Delrosso, D., Mattia, G., Fratianni, C., Storto, A., Ciliberti, S., Lemieux, B., Fenu, E., Simoncelli,
685 S., Drudi, M., Grandi, A., Padeletti, D., Di Pietro, P., Pinardi, N.: A 1/24 degree resolution Mediterranean analysis and
686 forecast modelling system for the Copernicus Marine Environment Monitoring Service. Extended abstract to the 8th
687 EuroGOOS Conference, Bergen, http://eurogoos.eu/download/publications/EuroGOOS-2017-Conference-Proceedings.pdf,
688 2017b.

690 Clementi, E., Pistoia, J., Escudier, R., Delrosso, D., Drudi, M., Grandi, A., Lecci, R., Cretí, S., Ciliberti, S., Coppini, G.,
691 Masina, S., Pinardi, N.: Mediterranean Sea Analysis and Forecast (CMEMS MED-Currents EAS5 system, 2017-2020)
692 [Data set]. Copernicus Monitoring Environment Marine Service (CMEMS),
693 https://doi.org/10.25423/CMCC/MEDSEA_ANALYSIS_FORECAST_PHY_006_013_EAS5, 2019.

695 Copin-Montegut, C.: Alkalinity and carbon budgets in the Mediterranean Sea. Global Biogeochemical Cycles, 7(4), pp. 915-
696 925, 1993.

697 Copernicus Marine In-Situ Team and Copernicus In Situ TAC, Real Time Quality Control for WAVES. CMEMS-INS-
698 WAVES-RTQC. https://doi.org/10.13155/46607, 2020.

699 Cossarini, G., Mariotti, L., Feudale, L., Teruzzi, A., D'Ortenzio, F., Tallandier, V., and Mignot A.: Towards operational 3D-
700 Var assimilation of chlorophyll Biogeochemical-Argo float data into a biogeochemical model of the Mediterranean Sea,
701 Ocean Model, 133, 112–128, https://doi.org/10.1016/j.ocemod.2018.11.005, 2019.

703 Cossarini G., Lazzari P., and Solidoro, C.: Spatiotemporal variability of alkalinity in the Mediterranean Sea, Biogeosciences,
704 12, 1647–1658, https://doi.org/10.5194/bg-12-1647-2015, 2015.

706 Cossarini G., Bretagnon M., Di Biagio V., Fanton d'Andon O., Garnesson P., Mangin A., and Solidoro C.: Primary
707 production. In: Copernicus Marine Service Ocean State Report, Issue 3, J. Oper. Oceanogr., 12:sup1, s88–s91; DOI:
708 10.1080/1755876X.2020.1785097, 2020.

710 Deliverable D4.6: SES land-based runoff and nutrient load data (1980 2000), edited by Bouwman L. and van Apeldoorn D.,
711 2012 PERSEUS H2020 grant agreement n. 287600.

713 Delrosso, D.: Numerical modelling and analysis of riverine influences in the Mediterranean Sea, PhD Thesis, Alma Mater
714 Studiorum Università di Bologna. DOI 10.6092/unibo/amsdottorato/9392, 2020.

716 Desroziers, G., Berre, L., Chapnik, B. and Poli, P.: Diagnosis of observation, background and analysis-error statistics in
717 observation space. Q.J.R. Meteorol. Soc. 131: 3385–3396. doi: 10.1256/qj.05.108, 2005.

Dobricic, S. and Pinardi, N.: An oceanographic three-dimensional variational data assimilation scheme, Ocean modelling, 22: 89-105 (2008), doi:10.1016/j.ocemod.2008.01.004, 2008.

Dobricic, S., Pinardi, N., Adani, M., Tonani, M., Fratianni, C., Bonazzi, A., and Fernandez, V.: "Daily oceanographic analyses by the Mediterranean basin scale assimilation system, Ocean Sciences, 3, 149-157, doi:10.5194/os-3-149-2007, 2007.

Dobricic, S., Dufau C., Oddo P., Pinardi N., Pujol I., and Rio M.-H.: Assimilation of SLA along track observations in the Mediterranean with an oceanographic model forced by atmospheric pressure. Ocean Sci., 8, 787-795, doi:10.5194/os-8-787-2012, 2012.

Dobricic, S., Pinardi N., Testor P. and Send U.: Impact of data assimilation of glider observations in the Ionian Sea (Eastern Mediterranean), Dynamics of Atmospheres and Oceans, 50, 78-92, doi:10.1016/j.dynatmoce.2010.01.001, 2010.

ECMWF IFS Documentation CY43R1, Part VII: ECMWF Wave Model, Book chapter, ECMWF, 2016.

Escudier, R., Clementi, E., Omar, M., Cipollone, A., Pistoia, J., Aydogdu, A., Drudi, M., Grandi, A., Lyubartsev, V., Lecci, R., Cretí, S., Masina, S., Coppini, G., Pinardi, N.: Mediterranean Sea Physical Reanalysis (CMEMS MED-Currents) (Version 1) [Data set]. Copernicus Monitoring Environment Marine Service (CMEMS), https://doi.org/10.25423/CMCC/MEDSEA_MULTIYEAR_PHY_006_004_E3R1, 2020.

Escudier, R., Clementi, E., Cipollone, A., Pistoia, J., Drudi, M., Grandi, A., Lyubartsev, V., Lecci, R., Aydogdu, A., Delrosso, D., Omar, M., Masina, S., Coppini, G., Pinardi. N.: A High Resolution Reanalysis for the Mediterranean Sea. Front. Earth Sci. 9:702285. doi: 10.3389/feart.2021.702285, 2021.

Fennel, K., Gehlen, M., Brasseur, P., Brown, C.W., Ciavatta, S., Cossarini, G., Crise A., Edwards, C.A., Ford, D., Friedrichs, M.A.M., Gregoire, M., Jones, E., Kim, H.C., Lamouroux, J., Murtugudde, R., Perruche, C.: Advancing Marine Biogeochemical and Ecosystem Reanalyses and Forecasts as Tools for Monitoring and Managing Ecosystem Health. Front. Mar. Sci., 6, UNSP 89, doi: 10.3389/fmars.2019.00089, 2019.

Feudale, L., Bolzon, G., Lazzari, P., Salon, S., Teruzzi, A., Di Biagio, V., Coidessa, G., & Cossarini, G.: Mediterranean Sea Biogeochemical Analysis and Forecast (CMEMS MED-Biogeochemistry, MedBFM3 system) (Version 1) [Data set]. Copernicus Monitoring Environment Marine Service (CMEMS). https://doi.org/10.25423/CMCC/MEDSEA_ANALYSISFORECAST_BGC_006_014_MEDBFM3 2021.

Fourrier M., Coppola L., Claustre H., D'Ortenzio F., Sauzède R., Gattuso, J-P.: A Regional Neural Network Approach to Estimate Water-Column Nutrient Concentrations and Carbonate System Variables in the Mediterranean Sea: CANYON-MED. Front. Mar. Sci. 2020, 7, 620, 2021.

Giesen, R., Clementi, E., Bajo, M., Federico, I., Stoffelen, A., Santoleri R.: The November 2019 record high water levels in Venice, Italy. In: Copernicus Marine Service Ocean State Report, Issue 5, Journal of Operational Oceanography, 14:sup1, s140–s148; DOI: 10.1080/1755876X.2021.1946240, 2021.

Gunther, H., Hasselmann, H., and Janssen, P.A.E.M.: The WAM model cycle 4, DKRZ report n. 4, 1993.

Janssen, P.A.E.M.: Wave induced stress and the drag of air flow over sea wave, J. Phys. Ocean., 19, 745-754, 1989.

Janssen, P.A.E.M.: Quasi-Linear theory of wind wave generation applied to wave forecasting, J. Phys. Ocean., 21, 1631-1642, 1991.

Johnson, K., Pasqueron De Fommervault, O., Serr, R., D'Ortenzio, F., Schmechtig, C., Claustre, H., and Poteau A.: Processing Bio-Argo nitrate concentration at the DAC Level. Version 1.1, March 3rd, IFREMER for Argo Data Management, 22pp. DOI: http://doi.org/10.13155/46121, 2018.

Hasselmann, K., On the spectral dissipation of ocean waves due to whitecapping, Boundary-Layer Meteorol., 126, 107 – 127, 1974.

Hasselmann K., Allender J. H., and Barnett, T. P.: Computations and parameterizations of the nonlinear energy transfer in a gravity wave spectrum. Part II: Parameterizations of the nonlinear energy transfer for application in wave models. J. Phys. Oceanogr.,15, 1378–1391, 1985.

Hasselmann, K., Hasselmann, K., Barnett, T.P., Bouws, E., Carlson, H., Cartwright, D.E., Enke, K., Ewing, J.A., Gienapp, H., Hasselmann, D.E., Kruseman, P., Meerburg, A., Müller, P., Olbers, D.J., Richter, K., Sell, W., Walden, H.: Measurements of wind–wave growth and swell decay during the Joint North Sea Wave Project (JONSWAP), Dtsch. Hydrogr. Z., 8, 1–95, 1973.

Hernandez, F., Bertino, L., Brassington, G., Chassignet, E., Cummings J., Davidson F., Drévillon, M., G. Garric, M. Kamachi, J.-M. Lellouche, R. Mahdon, M.J. Martin, A. Ratsimandresy, and C. Regnier,: Validation and intercomparison studies within GODAE. Oceanography 22(3): 128–143, https://doi.org/10.5670/oceanog.2009.71, 2009.

Hernandez, F., Smith, G., Baetens, K., Cossarini, G., Garcia-Hermosa, I., Drevillon, M., Maksymczuk, J., Melet, A., Regnier, C., Von Schuckman, K.: Measuring Performances, Skill and Accuracy in Operational Oceanography: New Challenges and Approaches, New Frontiers in Operational Oceanography, E. Chassignet, A. Pascual, J. Tintoré, and J. Verron, Eds., GODAE OceanView, 759-796, doi:10.17125/gov2018.ch29, 2018.

Katsafados, P., Papadopoulos, A., Korres, G., Varlas, G.: A fully coupled Atmosphere–Ocean Wave modeling system (WEW) for the Mediterranean Sea: interactions and sensitivity to the resolved scales and mechanisms, Geosci. Model Dev., 9, 161–173, 2016.

Kempe, S., Pettine M., and Cauwet, G.: Biogeochemistry of european rivers. In Degensempe & Richey eds, biogeochemistry of Major World Rivers, SCOPE 42 John Wiley 169-211, 1991.

Komen, G.J., Hasselmann, S., and Hasselmann, K.: On the existence of a fully developed windsea spectrum, J. Phys. Ocean., 14, 1271-1285, 1984.

Komen, G. J., Cavaleri, L., Donelan, M., Hasselmann, K., Hasselmann, S., and Janssen, P.: Dynamics and modelling of ocean waves, Cambridge University Press, Cambridge, 1994.

Krasakopoulou, E., Souvermezoglou, E., Giannoudi, L., Goyet, C.: Carbonate system parameters ad anthropogenic CO_2 in the North Aegean Sea during October 2013. Continental Shelf Research, 149, 69-81, 2017.

Lazzari, P., Teruzzi, A., Salon, S., Campagna, S., Calonaci, C., Colella, S., Tonani, M., Crise, A: Pre-operational short-term forecasts for the Mediterranean Sea biogeochemistry, Ocean Sci., 6, 25–39, https://doi.org/10.5194/os-6-25-2010, 2010.

Lazzari, P., Solidoro, C., Ibello, V., Salon, S., Teruzzi, A., Branger, K., Colella, S.; Crise, A.: Seasonal and inter-annual variability of plankton chlorophyll and primary production in the Mediterranean Sea: a modelling approach. Biogeosciences 2012, 9:217–233, doi:10.5194/bg-9-217-2012, 2012.

Lazzari, P., Solidoro, C., Salon, S., Bolzon, G.: Spatial variability of phosphate and nitrate in the Mediterranean Sea: a modelling approach. Deep-Sea Res. Pt. I, 108, 39–52, https://doi.org/10.1016/j.dsr.2015.12.006, 2016.

Lazzari, P., Álvarez, E., Terzić, E., Cossarini, G., Chernov, I., D'Ortenzio, F., Organelli, E.: CDOM Spatiotemporal Variability in the Mediterranean Sea: A Modelling Study. *J. Mar. Sci. Eng.*, 9(2), 176, 2021.

Lionello, P., H. Gunther, and P. A. E. M., Janssen: Assimilation of altimeter data in a global third generation wave model. J. Geophys. Res., 97C, 14 453–14 474, 1992.

825
826 Lellouche, J.-M., Greiner, E., Le Galloudec, O., Garric, G., Regnier, C., Drevillon, M., Benkiran, M., Testut, C.E.,
827 Bourdalle-Badie, R., Gasparin, F., Hernández, O., Levier, B., Drillet, Y., Remy, E., Le Traon, P.Y.: Recent updates on the
828 Copernicus Marine Service global ocean monitoring and forecasting real-time 1/12° high resolution system. Ocean Sci.
829 Discuss. doi: https://doi.org/10.5194/os-2018-15, 2018.
830
831 Lermusiaux, O.F.J.: Evolving the subspace of the three-dimensional multiscale ocean variability: Massachusetts Bay. Journal
832 of Marine Systems 29, 385–422, https://doi.org/10.1016/S0924-7963(01)00025-2 2001.
833
834 Le Traon, P. Y., Reppucci, A., Alvarez Fanjul, E., Aouf, L., Behrens, A., Belmonte, M., Bentamy, A., Bertino, L., Brando,
835 V., Kreiner, M.B., Benkiran, M., Carval, T., Ciliberti, S.A., Claustre, H., Clementi, E., Coppini, G., Cossarini, G., De
836 Alfonso Alonso-Muñoyerro, M., Delamarche, A., Dibarboure, G., Dinessen, F., Drevillon, M., Drillet, Y., Faugere, Y.,
837 Fernández, V., Fleming, A., Garcia-Hermosa, M.I., Sotillo, M.G., Garric, G., Gasparin, F., Giordan, C., Gehlen, M.,
838 Gregoire, M.L., Guinehut, S., Hamon, M., Harris, C., Hernandez, F., Hinkler, J.B., Hoyer, J., Karvonen, J., Kay, S., King,
839 R., Lavergne, T., Lemieux-Dudon, B., Lima, L., Mao, C., Martin, M.J., Masina, S., Melet, A., Buongiorno Nardelli, B.,
840 Nolan, G., Pascual, A., Pistoia, J., Palazov, A., Piolle, J.F., Pujol, M.I., Pequignet, A.C., Peneva, E., Pérez Gómez, B., Petit
841 de la Villeon, L., Pinardi, N., Pisano, A., Pouliquen, S., Reid, R., Remy, E., Santoleri, R., Siddorn, J., She, J., Staneva, J.,
842 Stoffelen, A., Tonani, M., Vandenbulcke, L., von Schuckmann, K., Volpe, G., Wettre, C., and Zacharioudaki, A.: From
843 Observation to Information and Users: The Copernicus Marine Service Perspective. Front. Mar. Sci. 6:234. doi:
844 10.3389/fmars.2019.00234, 2019.
845
846 Levy, M., Estubier, A., Madec, G.: Choice of an advection scheme for biogeochemical models. Geophys. Res. Let., 28.
847 Madec, G. and the NEMO system Team. NEMO Ocean Engine, Scientific Notes of Climate Modelling Center (27) - ISSN
848 1288-1619, Institut Pierre-Simon Laplace (IPSL) 2019, http://doi.org/10.5281/zenodo.1464816 2001
849
850 Madec, G., Delecluse, P., Imbard, M., Levy, C.: OPA8.1 Ocean general Circulation Model reference m anual. Note du Pole
851 de modelisazion, Institut Pierre-Simon Laplace (IPSL), France, 11, 1998.
852
853 Maderich, V., Ilyin, Y., Lemeshko, E.: Seasonal and interannual variability of the water exchange in the Turkish Straits
854 System estimated by modelling. Mediterr. Mar. Sci., [S.l.], v. 16, n. 2, p. 444-459, ISSN 1791-6763,
855 doi:http://dx.doi.org/10.12681/mms.1103, 2015.
856
857 McEwan, R., Kay, S., Ford, D.: Quality Information Document of NWSHELF_ANALYSISFORECAST_BGC_004_002.
858 Marine Copernicus Service. https://catalogue.marine.copernicus.eu/documents/QUID/CMEMS-NWS-QUID-004-002.pdf,
859 accessed 15 July 2022, 2021.
860
861 McGovern, J.V., Dabrowski, T., Pereiro, D., Gutknecht, E., Lorente, P., Reffray, G., Aznar, R., Sotillo, M.G,: Quality
862 Information Document of IBI_ANALYSISFORECAST_BGC_005_004. Marine Copernicus Service.
863 https://catalogue.marine.copernicus.eu/documents/QUID/CMEMS-IBI-QUID-005-004.pdf, accessed 15 July 2022, 2020.
864
865 Melsom, A., Yumruktepe, Ç.: Quality Information Document of ARTIC_ANALYSIS_FORECAST_BIO_002_004. Marine
866 Copernicus Service. https://catalogue.marine.copernicus.eu/documents/QUID/CMEMS-ARC-QUID-002-004.pdf, accessed
867 15 July 2022, 2021.
868
869 Meybeck, M., Ragu, A.: River Discarges to the Oceans: An Assessment of suspended solids, major ions and nutrients UNEP
870 STUDY, 1995.
871
872 Milliff ,R., Bonazzi, A., Wikle, C.K., Pinardi, N., Berliner, L. M.: Ocean ensemble forecasting. Part I: Ensemble
873 Mediterranean winds from a Bayesian hierarchical model. Q. J. R. Meteorol. Soc. 137: 858–878. DOI:10.1002/qj.767, 2011.
874
875 Nagy, H., Lyons, K., Nolan, G., Cure, M., Dabrowski, T.: A Regional Operational Model for the North East Atlantic: Model
876 Configuration and Validation. J. Mar. Sci. Eng., 8, 673. https://doi.org/10.3390/jmse8090673, 2020.
877

878 Oddo, P., Adani, M., Pinardi, N., Fratianni, C., Tonani, M., Pettenuzzo, D.: A Nested Atlantic-Mediterranean Sea General
879 Circulation Model for Operational Forecasting. Ocean Sci., 5, 461-473, doi:10.5194/os-5-461-2009, 2009.
880
881 Oddo, P., Bonaduce, A., Pinardi, N., and Guarnieri, A.: Sensitivity of the Mediterranean sea level to atmospheric pressure
882 and free surface elevation numerical formulation in NEMO, Geosci. Model Dev., 7, 3001–3015. doi:10.5194/gmd-7-3001-
883 2014, 2014.
884
885 Pacanowski, R. C., and Philander, S. G. H.: Parameterization of vertical mixing in numerical models of tropical
886 oceans. Journal of Physical Oceanography, 11, 1443–1451. https://doi.org/10.1175/1520-
887 0485(1981)011<1443:POVMIN>2.0.CO;2, 1981.
888
889 Pettenuzzo, D., Large, W. G., Pinardi, N.: On the corrections of ERA-40 surface flux products consistent with the
890 Mediterranean heat and water budgets and the connection between basin surface total heat flux and NAO. J. Geophys. Res.,
891 115 (C6), doi:10.1029/ 2009JC005631, URL http://dx.doi.org/10.1029/2009JC005631, 2010.
892
893 Pinardi, N., Arneri, E., Crise, A., Ravaioli, M., and Zavatarelli, M.: "The physical, sedimentary and ecological structure and
894 variability of shelf areas in the Mediterranean Sea" The Sea, Vol. 14 (A. R. Robinson and K. Brink Eds.), Harvard
895 University Press, Cambridge, USA 1243-1330, 2006.
896
897 Pinardi, N., and Coppini, G.: Preface "Operational oceanography in the Mediterranean Sea: the second stage of
898 development", Ocean Sci., 6, 263–267, https://doi.org/10.5194/os-6-263-2010, 2010.
899
900 Pinardi, N., Zavatarelli, M., Adani, M., Coppini, G., Fratianni, C., Oddo, P., Simoncelli, S., Tonani, M., Lyubartsev, V.,
901 Dobricic, S., Bonaduce, A.: Mediterranean Sea large-scale low-frequency ocean variability and water mass formation rates
902 from 1987 to 2007: A retrospective analysis. Prog. Oceanogr, 132, 318–332, https://doi.org/10.1016/j.pocean.2013.11.003,
903 2015.
904
905 Pinardi, N., Lermusiaux, P., F. J.; Brink Kenneth, H., Preller Ruth, H.: The Sea: The science of ocean predictions. Journal of
906 Marine Research, Volume 75, Number 3, May 2017, pp. 101-102(2), 10.1357/002224017821836833, 2017.
907
908 Pinardi, N., Cessi, P., Borile, F., Wolfe, C.L.: The Mediterranean Sea Overturning Circulation. J. Phys. Oceanogr., 49, 1699–
909 1721, doi: 10.1175/JPO-D-18-0254.1, 2019.
910
911 Pistoia, J., Clementi, E., Delrosso, D., Mattia, G., Fratianni, C., Drudi, M., Grandi, A., Padeletti, D., Di Pietro, P., Storto, A.,
912 Pinardi., N.: Last improvements in the data assimilation scheme for the Mediterranean Analysis and Forecast system of the
913 Copernicus Marine Service. Extended abstract to the 8th EuroGOOS Conference 2017, Bergen,
914 http://eurogoos.eu/download/publications/EuroGOOS-2017-Conference-Proceedings.pdf, 2017.
915
916 Ramirez-Romero, E., Jordà, G., Amores, A., Kay, S., Segura-Noguera, M., Macias, D.M., Maynou, F., Sabatés, A., and
917 Catalán, I.A.: Assessment of the Skill of Coupled Physical–Biogeochemical Models in the NW Mediterranean.
918 Front. Mar. Sci. 7:497. doi: 10.3389/fmars.2020.00497, 2020.
919
920 Ravdas, M., Zacharioudaki, A., Korres, G.: Implementation and validation of a new operational wave forecasting system of
921 the Mediterranean Monitoring and Forecasting Centre in the framework of the Copernicus Marine Environment Monitoring
922 Service. Nat. Hazards Earth Syst. Sci., 18, 2675-2695, https://doi.org/10.5194/nhess-18-2675-2018, 2018.
923
924 Ribera d'Alcalà, M., Civitarese, G., Conversano, F., Lavezza, R.: Nutrient ratios and fluxes hint at overlooked processes in
925 the Mediterranean Sea. Journal of Geophysical Research, 108(C9), 8106, doi:10.1029/2002JC001650, 2003.
926
927 Robinson, A.R., Leslie, W.G., Theocharis, A., Lascartos, A.: Mediterranean Sea Circulation. Encyclopedia of Ocean
928 Sciences, pp 1689-1705, https://doi.org/10.1006/rwos.2001.0376, 2001.
929

930 Salon, S., Cossarini, G., Bolzon, G., Feudale, L., Lazzari, P., Teruzzi, A., Solidoro, C., Crise, A.: Marine Ecosystem
931 forecasts: skill performance of the CMEMS Mediterranean Sea model system. Ocean Sci. Discuss., 1–35,
932 https://doi.org/10.5194/os-2018-145, 2019.

934 Schneider, A., Wallace, D. W. R., and Kortzinger, A.: Alkalinity of the Mediterranean Sea, Geophys. Res. Lett., 34, L15608,
935 doi:10.1029/2006GL028842, 2007.

937 Schmechtig, C., Poteau, A., Claustre, H., D'Ortenzio, F., Dall'Olmo, G., Boss, E.: Processing Bio-Argo particle
938 backscattering at the DAC level. https://doi.org/10.13155/39468, 2018.

940 Semedo, A., Sušelj, K, Rutgersson, A., and Sterl, A.: A global view on the wind sea and swell climate and variability from
941 EERA-40 J. Clim. 24 1461–79, 2011.

943 Simoncelli, S., Masina, S., Axell, L., Liu, Y., Salon, S., Cossarini, G., Bertino, L., Xie, J., Samuelsen, A., Levier, B., et al.:
944 MyOcean regional reanalyses: overview of reanalyses systems and main results. Mercator Ocean J 54: Special issue on main
945 outcomes of the MyOcean2 and MyOcean follow-on projects. https://www.mercator-
946 ocean.fr/wpcontent/uploads/2016/03/JournalMO-54.pdf , 2016.

948 Simoncelli, S., Fratianni, C., Pinardi, N., Grandi, A., Drudi, M., Oddo, P., Dobricic, S.: Mediterranean Sea Physical
949 Reanalysis (CMEMS MED-Physics) (Version 1) [Data set]. Copernicus Monitoring Environment Marine Service
950 (CMEMS). https://doi.org/10.25423/MEDSEA_REANALYSIS_PHYS_006_004, 2019.

952 Siokou-Frangou, I., Christaki, U., Mazzocchi, M.G., Montresor, M., Ribera d'Alcal, M., Vaqu, D., Zingone, A.: Plankton in
953 the open Mediterranean Sea: a review. Biogeosciences, 7 (5):1543–1586, 2010.

955 Snyder, R. L., F. W. Dobson, J. A. Elliot, and R. B. Long: Array measurements of atmospheric pressure fluctuations above
956 surface gravity waves. J. Fluid Mech., 102, 1–59, 1981.

958 Sotillo, M.G., Campuzano, F., Guihou, K., Lorente, P., Olmedo, E., Matulka, A., Santos, F., Amo-Baladrón, M.A.,
959 Novellino, A.: River Freshwater Contribution in Operational Ocean Models along the European Atlantic Façade: Impact of a
960 New River Discharge Forcing Data on the CMEMS IBI Regional Model Solution. *J. Mar. Sci. Eng.* , *9*, 401.
961 https://doi.org/10.3390/jmse9040401, 2021

963 Souvermezoglou, E., Krasakopoulou, E., Pavlidou, A.: Temporal and spatial variability of nutrients and oxygen in the North
964 Aegean Sea during the last thirty years. Mediterranean Marine Science, 15/4, 805-822, 2014.

966 Spruch L ., Verjovkina, S., Jandt, S., Schwichtenberg, F., Huess, V., Lorkowski, I., Lagemaa, P.: Quality Information
967 Document of BALTICSEA_ANALYSIS_FORECAST_BIO_003_007. Marine Copernicus Service.
968 https://catalogue.marine.copernicus.eu/documents/QUID/CMEMS-BAL-QUID-003-007.pdf, accessed 15 July 2022, 2020.

970 Storto, A., Masina, S., Navarra, A.: Evaluation of the CMCC eddy-permitting global ocean physical reanalysis system (C-
971 GLORS, 1982-2012) and its assimilation components. Quarterly Journal of the Royal Meteorological Society, 142, 738–758,
972 doi: 10.1002/qj.2673, 2015.

974 Taburet, G., Sanchez-Roman, A., Ballarotta, M., Pujol, M.-I., Legeais, J.-F., Fournier, F.; Faugere, Y., Dibarboure, G.:
975 DUACSDT2018: 25years of reprocessed sea level altimetry products. Ocean Sci., 15, 1207–1224,
976 https://doi.org/10.5194/os-15-1207-2019, 2019.

978 Terzic, E., Salon, S., Solidoro, C., Cossarini, G., Teruzzi, A., Miro, A., Lazzari. P.: Impact of interannually variable diffuse
979 attenuation coefficients for downwelling irradiance on biogeochemical modelling. Ocean Modell., OCEMOD-D-20-
980 00012R2, 2021.
981

982   Teruzzi, A., Dobricic, S., Solidoro, C., and Cossarini, G.: A 3D variational assimilation scheme in coupled transport
983   biogeochemical models: Forecast of Mediterranean biogeochemical properties, J. Geophys. Res. Oceans, 119, 200–217,
984   https://doi.org/10.1002/2013JC009277, 2014.

986   Teruzzi, A., Bolzon, G., Salon, S., Lazzari, P., Solidoro, C., Cossarini, G.: Assimilation of coastal and open sea
987   biogeochemical data to improve phytoplankton modelling in the Mediterranean Sea. Ocean Model. 132, 46–60,
988   https://doi.org/10.1016/j.ocemod.2018.09.007, 2018.

990   Teruzzi, A., Di Cerbo, P., Cossarini, G., Pascolo, E., Salon, S.: Parallel implementation of a data assimilation scheme for
991   operational oceanography: the case of the OGSTM-BFM model system. Comput. Geosci., 124, 103–114,
992   https://doi.org/10.1016/j.cageo.2019.01.003, 2019.

994   Teruzzi, A., Bolzon, G., Feudale, L., Cossarini, G.: Deep chlorophyll maximum and nutricline in the Mediterranean Sea:
995   emerging properties from a multi-platform assimilated biogeochemical model experiment. Biogeosciences, 18(23), 6147-
996   6166, 2021.

998   Thoppil, P.G., Frolov, S., Rowley, C.D. et al.: Ensemble forecasting greatly expands the prediction horizon for ocean
999   mesoscale variability. Commun Earth Environ 2, 89 https://doi.org/10.1038/s43247-021-00151-5, 2021.

1001 Toledano, C., Ghantous, M., Lorente, P., Dalphinet, A., Aouf, L., Sotillo, M.G.: Impacts of an Altimetric Wave Data
1002 Assimilation Scheme and Currents-Wave Coupling in an Operational Wave System: The New Copernicus Marine IBI Wave
1003 Forecast Service. J. Mar. Sci. Eng.10, 457, https://doi.org/10.3390/jmse10040457, 2022.

1005 Tonani, M., Balmaseda, M., Bertino, L., Blockley, E., Brassington, G., Davidson, F., Drillet, Y., Hogan, P., Kuragano, T.,
1006 Lee, T., Mehra, A., Paranathara, F., Tanajura, CAS, Wang, H.: Status and future of global and regional ocean prediction
1007 systems. J Operational Oceanography 8:201-220, doi:10.1080/1755876X.2015.1049892, 2015.

1009 Tonani, M., Pinardi, N., Dobricic, S., Pujol, I., Fratianni, C.: A high-resolution free-surface model of the Mediterranean Sea.
1010 Ocean Sci., 4, 1-14, 2008.

1012 Trisolino, P., di Sarra, A., Sferlazzo, D., Piacentino, S.; Monteleone, F., Di Iorio, T., Apadula, F., Heltai, D., Lanza, A.,
1013 Vocino, A., Caracciolo di Torchiarolo, L., Bonasoni, P., Calzolari, F., Busetto, M., Cristofanelli, P.: Application of a
1014 Common Methodology to Select in Situ CO2 Observations Representative of the Atmospheric Background to an Italian
1015 Collaborative Network. Atmosphere, 12, 246. https://doi.org/10.3390/atmos12020246, 2021.

1017 Tugrul, S., Besiktepe, T., Salihoglu, I.: Nutrient exchange fluxes between the Aegean ad tBlack Seas through the Marmara
1018 Sea. Mediterranean Marine Science, 3/1, 33-42, 2002.

1020 Vandenbulcke L., Capet A., Grégoire M.: Quality Information Document of
1021 BLKSEA_ANALYSIS_FORECAST_BIO_007_010. Marine Copernicus Service.
1022 https://catalogue.marine.copernicus.eu/documents/QUID/CMEMS-BS-QUID-007-010.pdf, accessed 15 July 2022, 2021.

1024 Vichi M., Lovato, T., Butenschön, M., Tedesco, L., Lazzari, P., Cossarini, G., Masina, S., Pinardi, N., Solidoro, C.,
1025 Zavatarelli, M.: The Biogeochemical Flux Model (BFM): Equation Description and User Manual. BFM version 5.2. BFM
1026 Report series N. 1, Release 1.2, June 2020, Bologna, Italy, http://bfm-community.eu, pp. 104, 2020.

1028 Volpe, G., Colella, S., Brando, V. E., Forneris, V., Padula, F. L., Cicco, A. D., ... and Santoleri, R.: Mediterranean ocean
1029 colour Level 3 operational multi-sensor processing. Ocean Science, 15(1), 127-146, 2019.

1031 von Schuckmann, K., Le Traon P.-Y., […]: The Copernicus Marine Environment Monitoring Service Ocean State Report,
1032 Journal of Operational Oceanography, 9:sup2, s235-s320, DOI: 10.1080/1755876X.2016.1273446, 2016.
1033

1034   von Schuckmann K., […]: Copernicus Marine Service Ocean State Report, Journal of Operational Oceanography, 11:sup1,
1035   S1-S142, DOI: 10.1080/1755876X.2018.1489208, 2018.
1036
1037   von Schuckmann K., […]: Copernicus Marine Service Ocean State Report, Issue 3, Journal of Operational Oceanography,
1038   12:sup1, S1-S123, DOI: 10.1080/1755876X.2019.1633075, 2019
1039
1040   von Schuckmann, K., […]: Copernicus Marine Service Ocean State Report, Issue 4. J.Op. Oceanogr., 13,
1041   https://doi.org/10.1080/1755876X.2020.1785097, 2020.
1042
1043   WAMDI Group. The WAM model—a third generation ocean wave prediction model. J. Phys. Oceanogr., 18:1775–1810.
1044   https://doi.org/10.1175/1520-0485(1988)018<1775:TWMTGO>2.0.CO;2, 1988.
1045
1046   Wanninkhof, R.: Relationship between wind speed and gas exchange over the ocean revisited. Limnol. Oceanogr. Methods
1047   12, 351–362. https://doi.org/10.4319/lom.2014.12.351, 2014.
1048
1049   Yalcin, B., Artuz, M.L., Pavlidou, A., Cubuk, S., Dassenakis, M.: Nutrient dynamics and eutrophication in the Sea of
1050   Marmara: data from recent oceanographic research. Science of the Total Environment, 601-602, 405-424, 2017.
1051
1052   Young, I.R.: Seasonal variability of the global ocean wind and wave climate. Int. J. Climatol. 19, 931–950.
1053   doi:10.1002/(SICI)1097-0088(199907)19:93.0.CO;2-O, 1999.
1054
1055
1056
1057
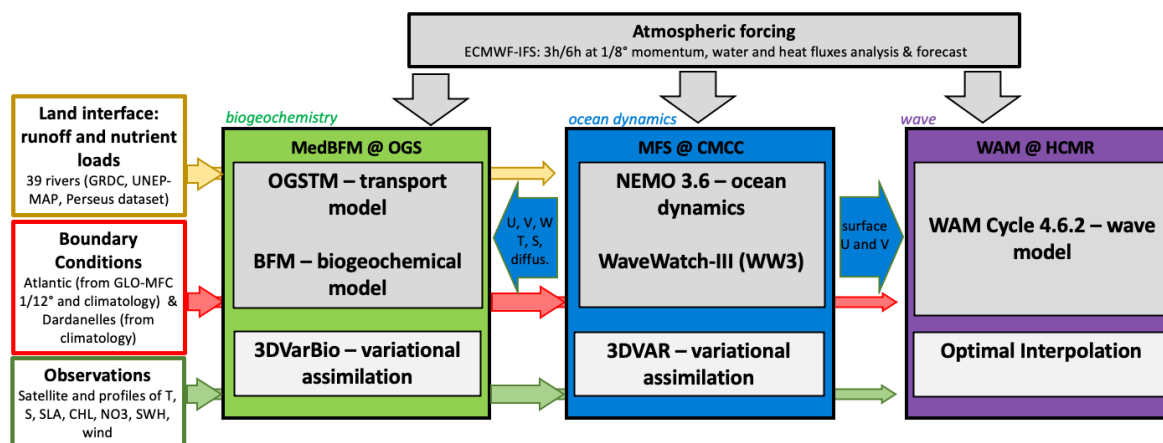
Figures

Figure 1: The Med-MFC core components and the off-line coupling scheme. The Blue arrow are the exchanged fields at daily frequency between the three components.

1066
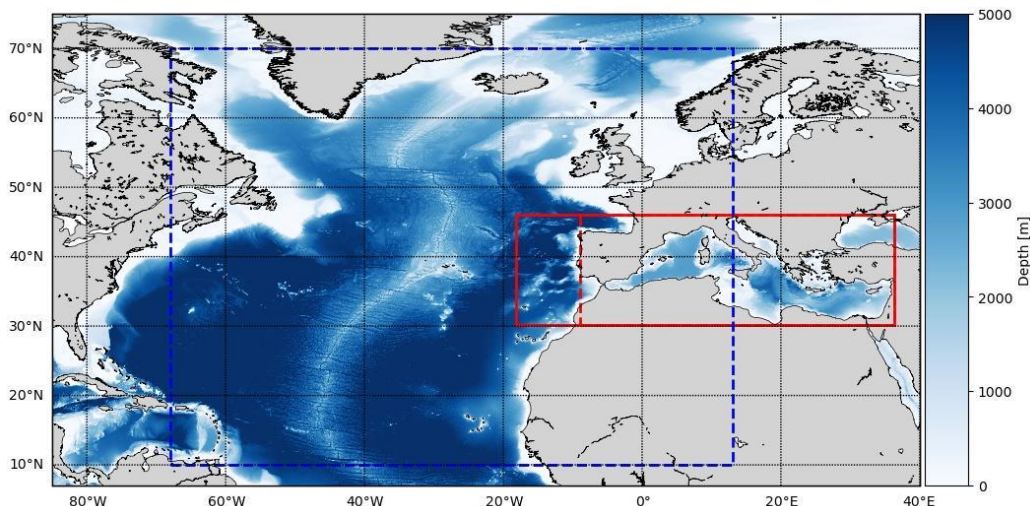
1067

1068 **Figure 2. The solid red box presents the domain of the PHY and WAV Mediterranean components. For BIO the domain extends in**
1069 **the Atlantic as far as the dashed red line. The blue box presents one of the WAM domains, producing boundary conditions for the**
1070 **Mediterranean WAV component which extends only in the solid red box.**

1071
1072
1073
1074
1075
1076
1077
1078
1079
1080
1081
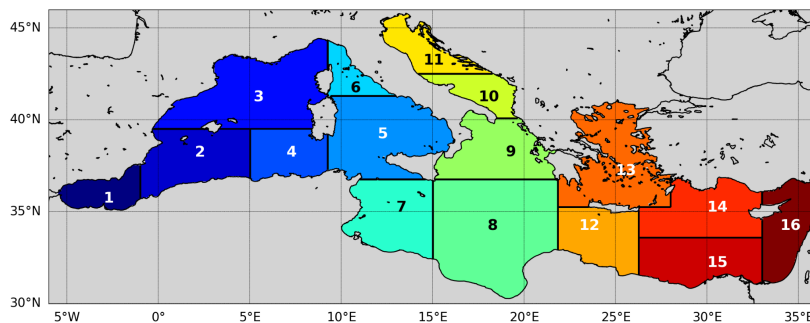
1082
1083 **Figure 3 The Mediterranean Sea domain and sub-regions subdivision for analysis of the skill scores: Alboran (1), South-West**
1084 **Mediterranean-1 (2), North-West Mediterranean (3), South-West Mediterranean-2 (4), South Tyrrenian (5), North Tyrrenian (6),**
1085 **West Ionian (7), East Ionian (8), North-East Ionian (9), South Adriatic (10), North Adriatic (11), West Levantine (12), Aegean (13),**
1086 **North-Central Levantine (14), South-Central Levantine (15), East Levantine (16).**

1087
1088
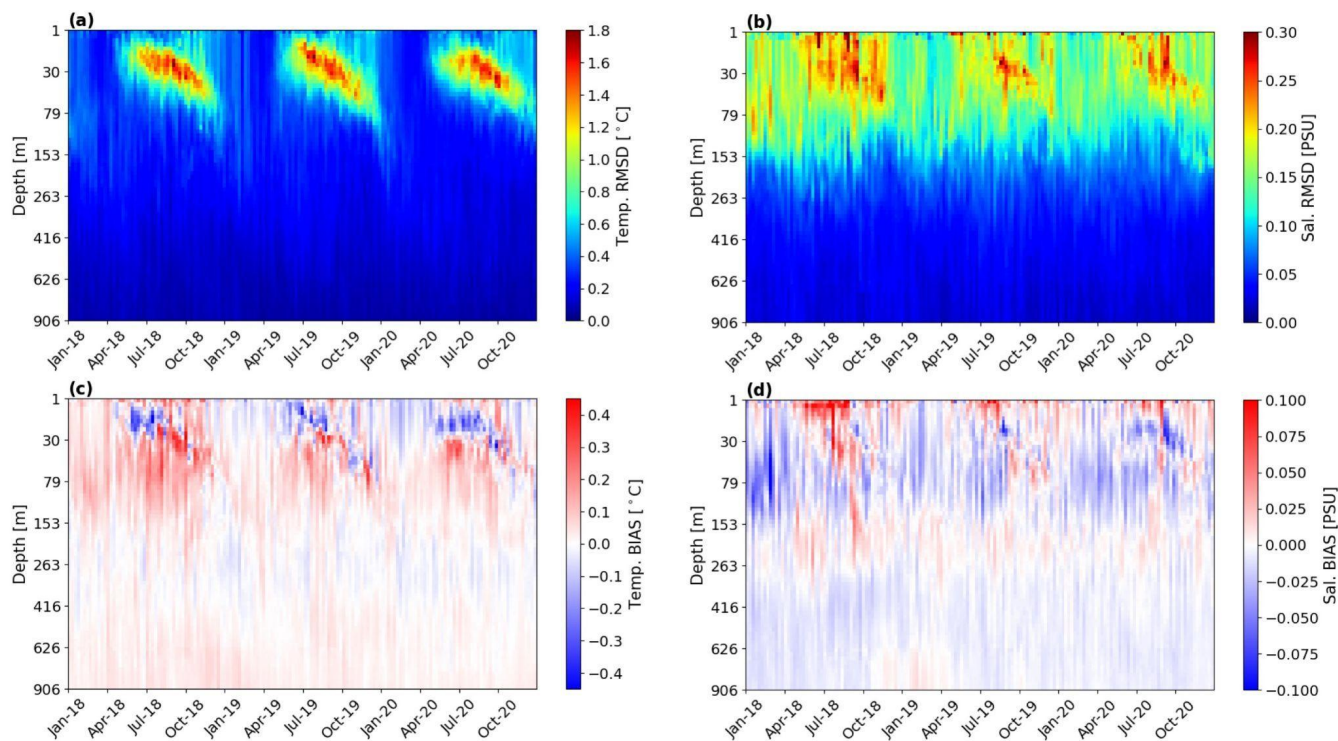
Figure 4 Hovmoller (Depth-Time) diagrams: (a) weekly RMS of temperature misfits, (b) weekly RMS salinity misfits, (c) weekly bias of temperature and (d) weekly bias of salinity, evaluated along the water column and averaged in the whole Mediterranean Sea.

1093

1094
1095
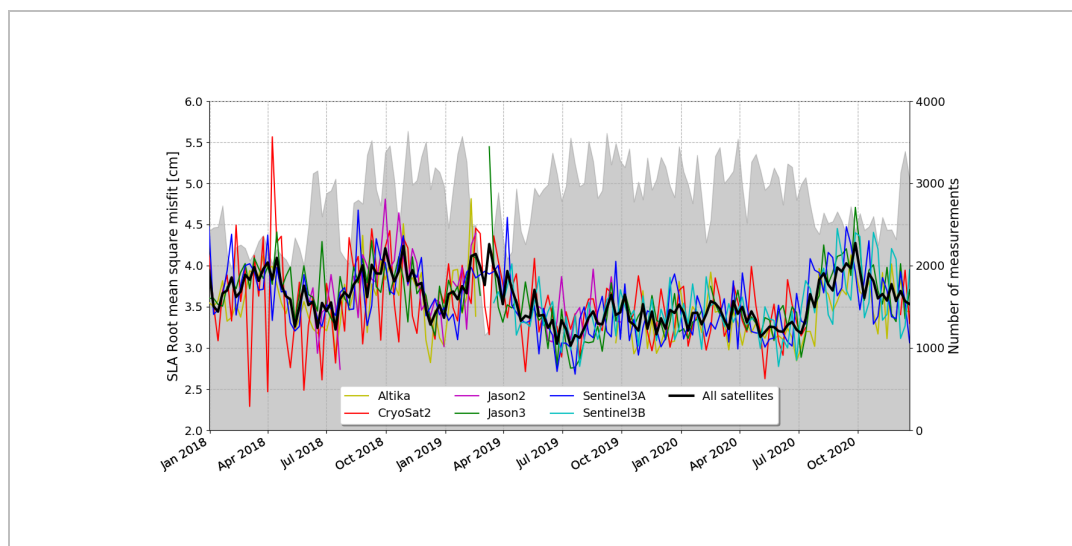
Figure 5. Time Series of weekly mean RMS misfit error for SLA evaluated with respect to available satellite altimeters and averaged in the whole Mediterranean Sea. Black bold line represents the mean error with respect to the whole set of satellites which are separately shown with different colours. The grey area indicates the number of observations used for the validation.

1099
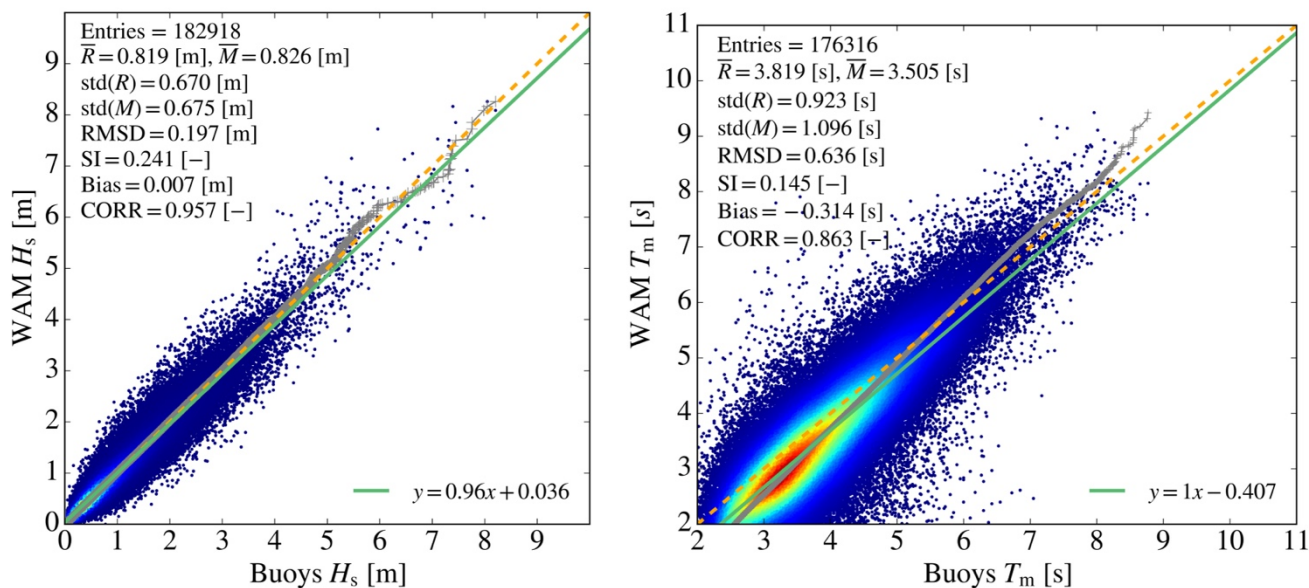
1100
1101 **Figure 6. Scatter plots of: (left) significant wave height (Hs); (right) mean wave period (Tm) versus wave buoy observations, for the**
1102 **28 stations of the Mediterranean Sea (bottom panel), for a three-year period (2018-2020). The graphs also include quantile-quantile**
1103 **plots (grey crosses), 45° reference lines (dashed orange line), and least-squares best fit lines (green line). On the top left of each**
1104 **picture statistical scores are given: entries refer to the number of data available for computing the statistics, R, M refer to the**
1105 **observed and modelled value respectively, SI is the Scatter Index (defined as the standard deviation of model-observation differences**
1106 **relative to the observed mean), and CORR is the Pearson correlation coefficient.**

1107
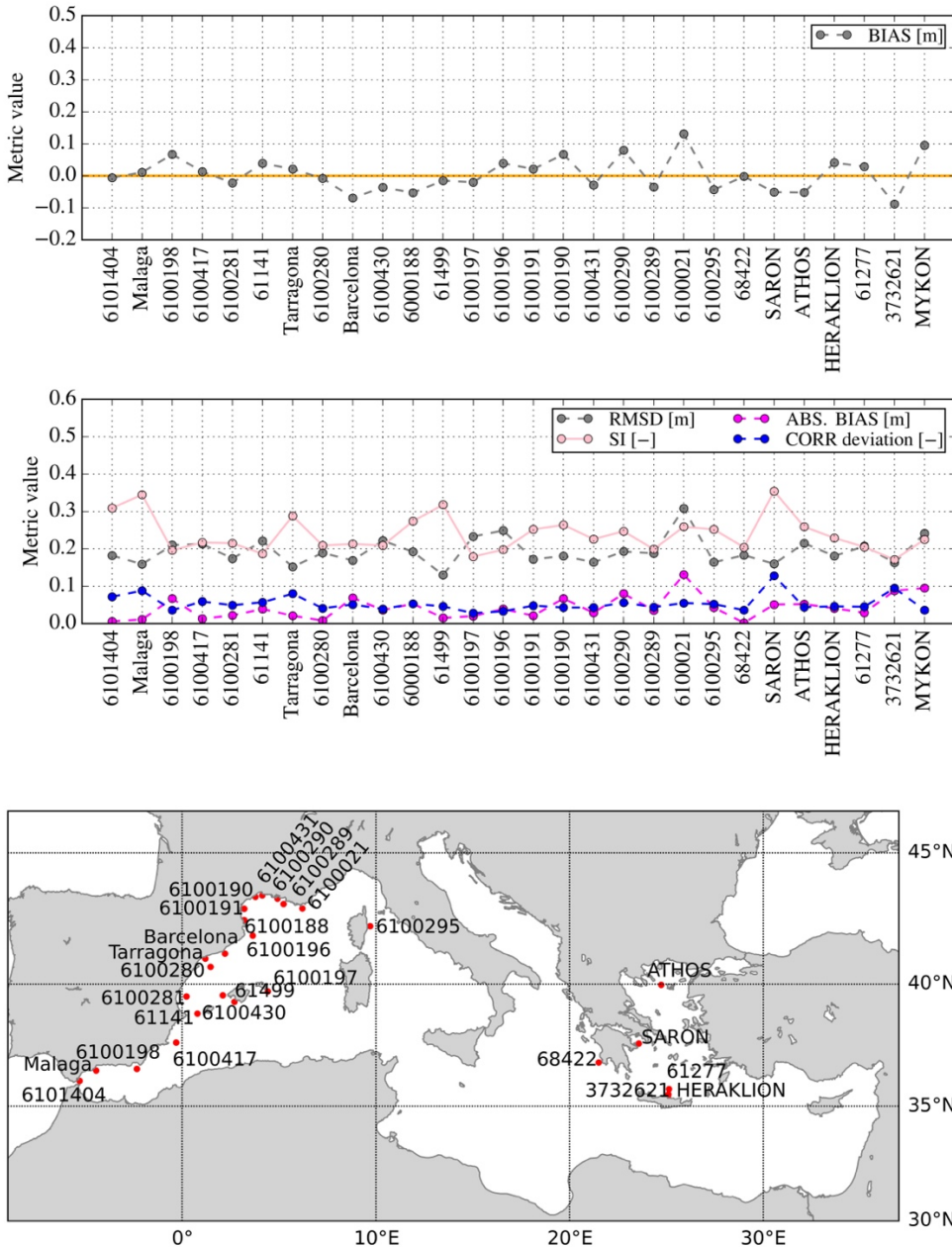
Figure 7. Significant wave height difference between model and observations (upper and middle graph) at the 28 buoy locations (lower panel) for a three-year period (2018-2020). For all locations, the performance of the model is evaluated against buoy data by means of bias, root mean square difference (RMSD), Scatter Index (SI), and deviations of the Pearson correlation coefficient from unity (CORR deviation).

1115

1116

1117

1118

1119

1120
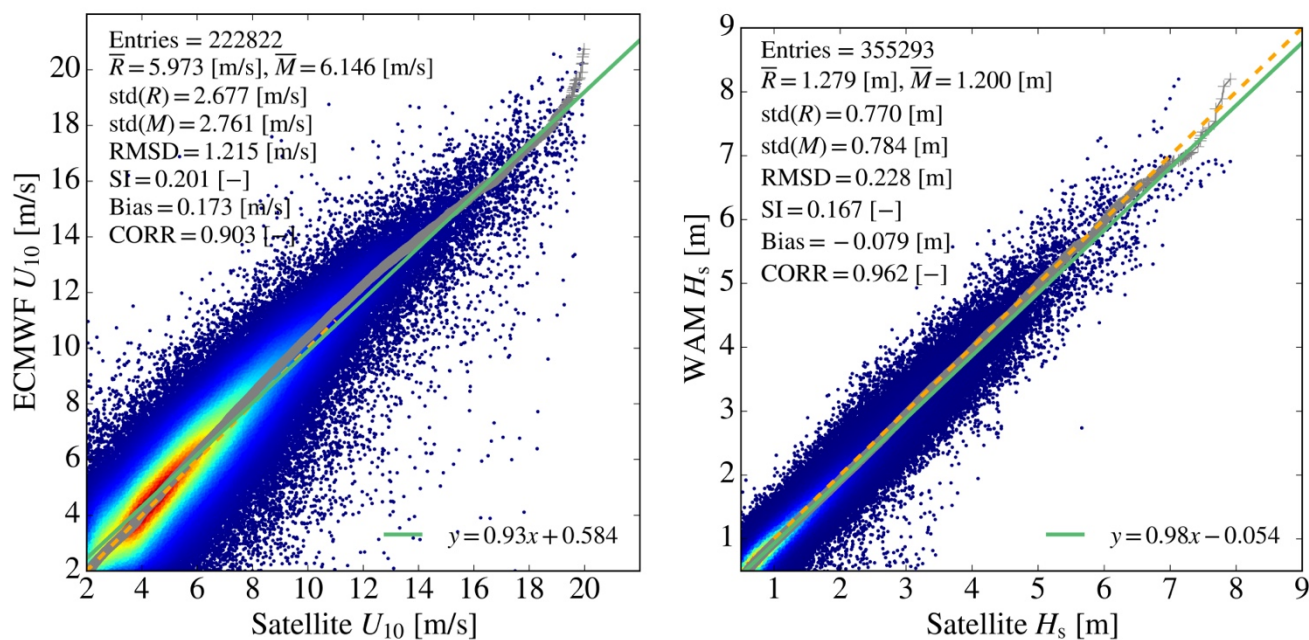
1121

1122

1123

Figure 8. Scatter plots of: ECMWF forcing wind speed U10 versus satellite U10 observations (left) and model significant wave height (Hs) versus satellite observations over the entire Mediterranean basin, for the three-year period (2018 – 2020).

1126

1127

1128
1129
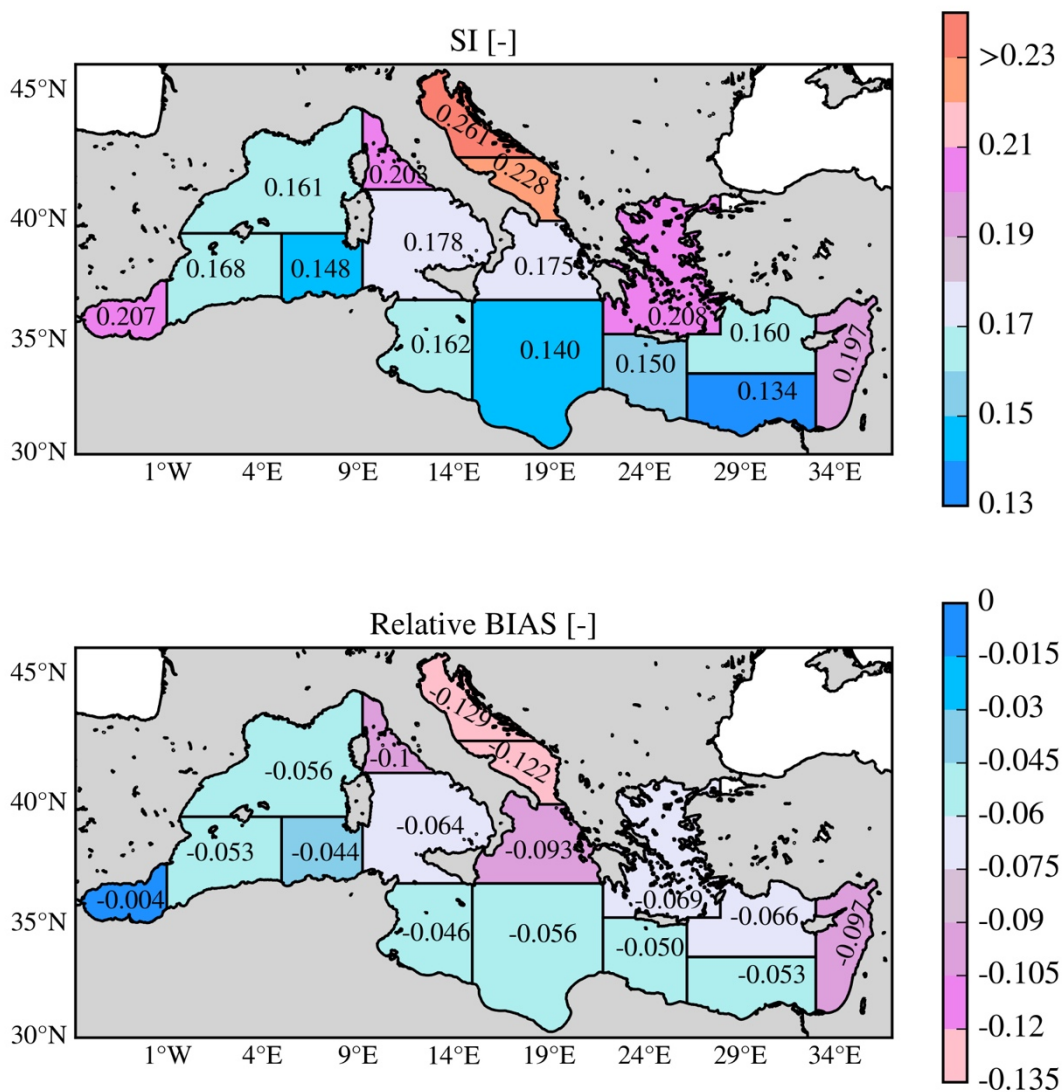
1130
1131 **Figure 9. SWH evaluation against satellite data: maps of Scatter Index (SI) (top) and Relative BIAS (bottom) over the Mediterranean**
1132 **Sea sub-regions (shown in Figure 3) for the three-year period (2018-2020).**

1133
1134
1135
1136

1137
1138
1139
1140
1141
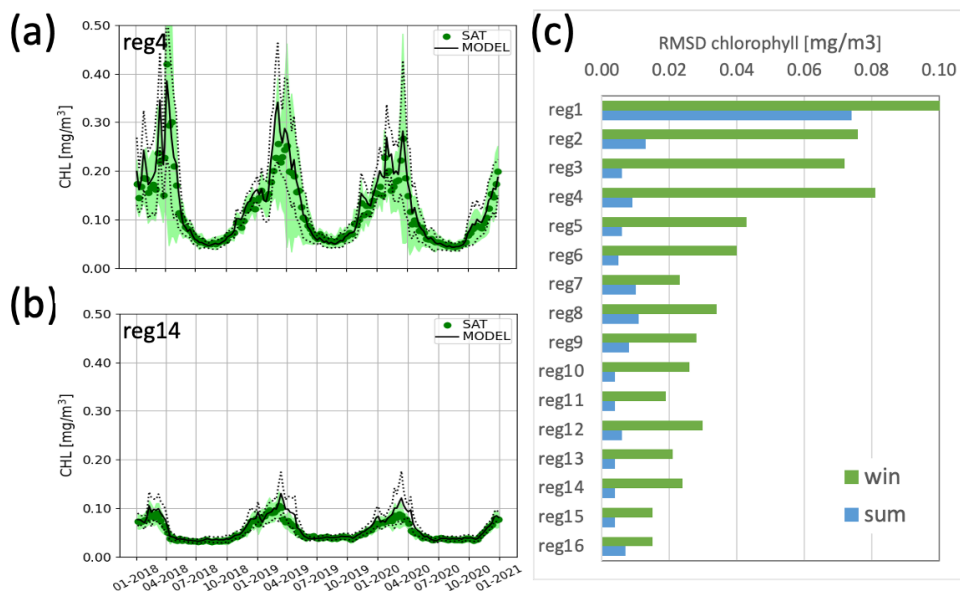
Figure 10. Timeseries of surface chlorophyll for centred composite 7-day satellite (green) and the model forecast (black) in two selected sub-regions (a and b). Mean winter (from Oct to Apr) and summer (from May to September) RMS of the differences between satellite and model forecast for the day before the assimilation in the 16 sub-regions of Fig.5(c).

1145

1146

1147

1148

1149

1150
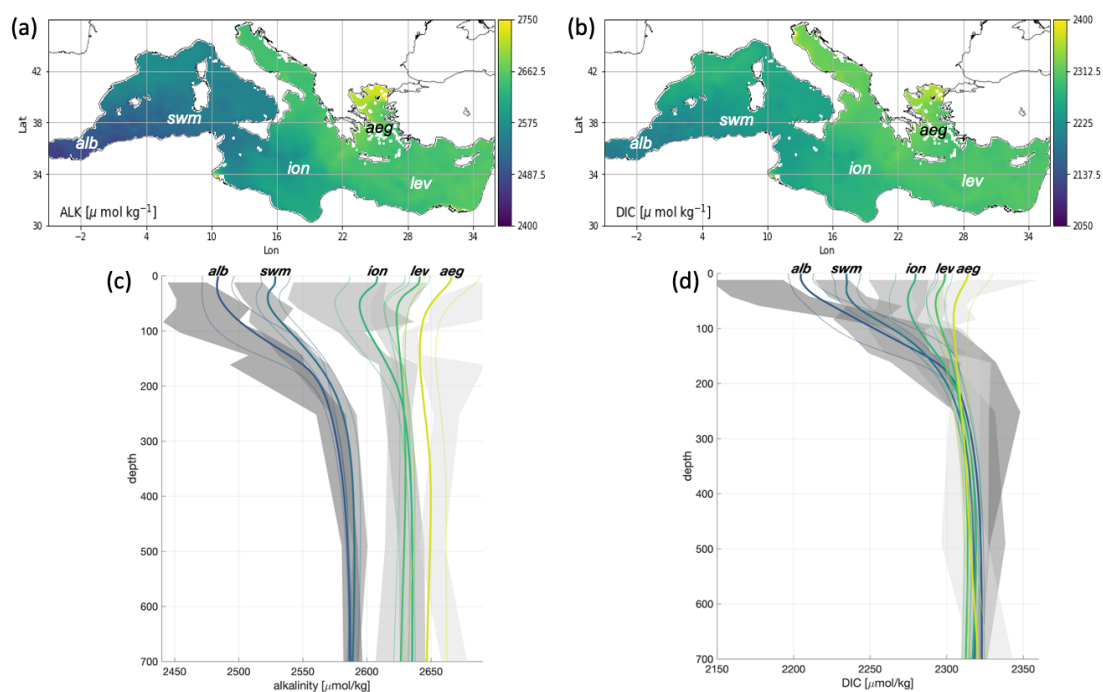
1151

Figure 11. spatial distribution of DIC (a) and alkalinity (b) and comparison of vertical profiles of DIC (c) and Alkalinity (d) for model (average and standard deviation coloured lines) and observed range of variability (grey shaded areas) for selected macro-areas. Climatological data are computed using historical data (Emodnet, 2018; Bakker 2014).

1155

1156
1157
1158 **Tables**
1159

1160 Table 1 Changes in the Mediterranean forecasting components since 2008.

Year	Numerical Model Changes
Physics component (PHY)	
< 2008	1/16 deg., 72 vert. lev., OPA8.2 model (Madec et al., 1998) with closed lateral boundary conditions in the Atlantic (Tonani et al., 2008), 7 rivers (Ebro, Rhone, Nile, Po, Seman, Vjiose, Buna-Bojana), closed lateral boundary at Dardanelles strait, OceanVar (Dobricic et al., 2007) weekly assimilation
2009	As in 2008 with NEMOv3.1 with climatological lateral open boundary conditions in the Atlantic (Oddo et al., 2009), OceanVar with daily assimilation (Dobricic et al., 2007)
2010	As in 2009 with one-way offline coupling between NEMOv3.1 and WAM (wave)
2013	As in 2010 with two-way coupling between NEMOv3.4 and WW3 (Clementi et al., 2017a)
2014	As in 2013 but with surface atmospheric pressure forcing (Oddo et al., 2014), explicit linear free surface and SLA TAPAS(*) data assimilation (Dobricic et al., 2012)
2015	As in 2014 but with daily lateral open boundary conditions in the Atlantic
2016	As in 2015 but with monthly and grid point EOF and vertical observational error varying with depth in OceanVar
2017	1/24 deg., 141 vert. lev., NEMOv3.6 with nonlinear free surface and z-star coordinate system), 39 rivers (Table A.4)
2019	As in 2017 but with open lateral boundary conditions at the Dardanelles Strait, improved SST nudging
Biogeochemistry component (BIO)	
<2008	1/8 deg BFM offline coupled to PHY component
2009	Offline coupling to horizontal subsampled PHY component at 1/8 deg
2013	Coupling with 1/16 deg PHY component and Biogeochemical Data Assimilation (BDA) for Ocean Color derived Chlorophyll data (Teruzzi et al., 2014)
2015	Inclusion of the carbonate system in the model (Cossarini et al., 2015)
2017	Revision nutrient formulation in BFM (Lazzari et al., 2016) and coupling with 1/24 deg PHY component including z-star coordinate system
2018	BDA for Ocean Color coastal data (Teruzzi et al., 2018)
2019	Open lateral boundary condition at the Dardanelles Strait, revision daily light cycle in BFM (Salon et al., 2019)
2020	Open lateral boundary condition in the Atlantic Ocean and BDA with Argo biogeochemical data (Cossarini et al., 2019), and daily operational 10-days of forecast
Wave component (WAV)	
2017	1/24 deg WAM Cycle 4.5.4, one-way offline coupled to PHY component surface currents. Open boundary conditions from North Atlantic implementation of WAM model at 1/6 deg resolution.
2018	Implementation of data assimilation for along track Significant Wave Height (SWH) observations from Jason 3 and Sentinel 3a

2019	WAM Cycle 4.6.2; assimilation of Cryosat-2 and Saral/Altika SWH observations tuning of wave age parameter; imposition of a limitation to the high frequency part of the spectrum based on Phillips spectrum.
2020	Assimilation of Sentinel-3b SWH observations t

(*) the Sea Level Anomaly (SLA) TAPAS product is produced to give information about the different corrections of the altimetric original signal.

Table 2. EAN estimates with in-situ observations. The differences (BIAS) and their square values (RMSD) are then averaged over the whole Mediterranean Sea region and 9 vertical layers for years 2018-2020.

Layer (m)	Temperature RMSD (°C)	Temperature bias (°C)	Salinity RMSD (PSU)	Salinity bias (PSU)
0-10	0.54	0.02	0.19	-0.01
10-30	0.82	0.04	0.20	0.01
30-60	0.85	-0.04	0.19	0.01
60-100	0.58	-0.03	0.16	0.02
100-150	0.41	0.01	0.13	0.01
150-300	0.28	0.02	0.08	0.02
300-600	0.18	0.00	0.05	0.01
600-1000	0.09	0.02	0.03	0.00
1000-2000	0.05	-0.01	0.02	0.00

Table 3. Gibraltar mean and standard deviation volume transports [Sv] from the Med-PHY numerical system averaged in the period 2018-2020 compared to literature values (current meter observations from October 2004 to January 2009).

Gibraltar Transport	Model [2018-2020]	Literature Soto-Navaro et al. (2010) [2004-2009]	Literature Candela (2001) [1994-1996]
Net	0.040±0.017	0.038 ± 0.007	0.04 (max: 0.26, min: 0.11)
Eastward	0.91±0.01	0.81 ± 0.06	1.01 (max: 1.12, min: 0.91)
Westward	0.087±0.06	0.78 ± 0.05	0.97 (max: 0.83, min: 1.11)

1182

1183   Table 4. EAN RMSD of SST and SLA averaged in the whole Mediterranean Sea and 16 sub-regions (see Figure 3) for the period
1184   2018-2020.

Region	Temperature RMSD (°C)	Sea Level Anomaly RMSD (cm)
MED SEA	0.54	3.8
REGION 1	0.69	5.3
REGION 2	0.53	4.3
REGION 3	0.53	3.2
REGION 4	0.55	5.1
REGION 5	0.47	3.1
REGION 6	0.49	3.5
REGION 7	0.51	5.0
REGION 8	0.55	3.8
REGION 9	0.51	3.4
REGION 10	0.58	2.3
REGION 11	0.63	NA
REGION 12	0.49	4.0
REGION 13	0.59	3.6
REGION 14	0.57	3.3
REGION 15	0.53	4.4
REGION 16	0.52	3.1

1185
1186
1187

1188

1189

1190

1191

1192

1193 Table 5. RMS of the difference between MedBFM and Argo-BGC profiles for ecosystem metrics. RMSD of the metrics are computed for
1194 each profile, then averaged over time and space considering the 2017-2020 period. Sub-regions: swm (reg2+reg4), nwm (reg3), tyr
1195 (reg5+reg6), adr (reg10+reg11), ion (reg7+reg8+reg9) and lev (reg13+reg14+reg15+reg16).

	vertical metrics [units]	mean value [range]	RMSD					
			swm	nwm	tyr	adr	ion	lev
Chlorophyll	Average 0-200m [mg/m3]	[0.01 - 1.5]	0.05	0.06	0.06	0.03	0.03	0.03
	Deep chlorophyll maximum depth [m]	80 [60-130]	10	11	7	6	16	18
	Mixed Bloom Winter depth [m]	40 [20-90]	25	39	35	29	16	27
Nitrate	Average 0-200m [mmol/m3]	[0.1-8.0]	-	0.72	0.45	-	0.52	0.54
	Nitracline depth [m]	90 [70-150]	-	48	44	-	34	42
Oxygen	Average 0-200m [mmol/m3]	220 [190-250]	11.5	8.5	7.9	10.8	4.7	5.7
	Maximum oxygen depth [m]	[60-120]	24	16	17	19	34	14

1196
1197
1198
1199

1200
1201

Table 6. RMSD of the difference between model and climatological profiles at different depths evaluated in the 2017-2020 reference period.

Statistics are computed using the 16 sub-regions in Figure 3.

Variable	indicative range values	RMSD							
		0-10	10-30	30-60	60-100	100-150	150-300	300-600	600-1000
Phosphate [mmol/m3] [2*]	0.01-0.70	0.092	0.03	0.027	0.023	0.043	0.028	0.040	0.027
Nitrate [mmol/m3][1*]	0.1-9.0	0.42	0.41	0.49	0.72	0.83	0.72	1.09	0.83
Ammonia [mmol/m3] [1*]	0.01-1.23	0.41	0.17	0.15	0.23	0.30	0.32	0.44	0.54
Silicate [mmol/m3] [1*]	0.1-8.0	1.5	1.5	1.3	0.9	0.9	0.7	0.7	0.8
Oxygen [mmol/m3] [1*]	190-260	5.9	5.7	6.4	4.2	5.23	4.3	8.6	5.8
DIC [μmol/kg] [1*]	2100-2400	42.2	37.6	28.1	17.1	16.7	7.7	9.9	3.8
Alkalinity [μmol/kg] [1*]	2360-2730	41.7	34.4	26.0	19.1	12.5	12.1	9.0	7.0
pH[1*]	7.0-8.2	0.04	0.03	0.03	0.02	0.01	0.01	0.01	0.01
pCO2 [μatm] [1**]	250-550	46							

1204
1205

---

[2] **Reference data for validation:** * EMODnet data collections (Buga et al., 2018) integrated with additional oceanographic cruises (Cossarini et al., 2015). ** Socat dataset (Baker et al 2014).